ADVANCED HEALTHCARE MATERIALS
www.advhealthmat.de

Gold-Enhanced Brachytherapy by a Nanoparticle-Releasing Hydrogel and 3D-Printed Subcutaneous Radioactive Implant Approach

*Mariia Kiseleva, Théophraste Lescot, Svetlana V. Selivanova, and Marc-André Fortin**

Brachytherapy (BT) is a widely used clinical procedure for localized cervical cancer treatment. In addition, gold nanoparticles (AuNPs) have been demonstrated as powerful radiosensitizers in BT procedures. Prior to irradiation by a BT device, their delivery to tumors can enhance the radiation effect by generating low-energy photons and electrons, leading to reactive oxygen species (ROS) production, lethal to cells. No efficient delivery system has been proposed until now for AuNP topical delivery to localized cervical cancer in the context of BT. This article reports an original approach developed to accelerate the preclinical studies of AuNP-enhanced BT procedures. First, an AuNP-containing hydrogel (Pluronic F127, alginate) is developed and tested in mice for degradation, AuNP release, and biocompatibility. Then, custom-made 3D-printed radioactive BT inserts covered with a AuNP-containing hydrogel cushion are designed and administered by surgery in mice (HeLa xenografts), which allows for measuring AuNP penetration in tumors (≈100 µm), co-registered with the presence of ROS produced through the interactions of radiation and AuNPs. Biocompatible AuNPs-releasing hydrogels could be used in the treatment of cervical cancer prior to BT, with impact on the total amount of radiation needed per BT treatment, which will result in benefits to the preservation of healthy tissues surrounding cancer.

1. Introduction

Cervical cancer represents the fourth most common malignancy in the world among women, with more than 300 000 deaths annually (2020 figures).[1] Despite the deployment of screening and prevention programs, cervical cancer mortality has remained stable for the past four decades.[2] Moreover, in 2021, the recurrence rates of cervical cancer were estimated to be 11–22% for women with stage IB-IIA cancers and 28–64% for those diagnosed with stage IIB-IVA cancers (classification according to the International Federation of Gynecology and Obstetrics).[3,4]

Current treatments of cervical cancer drastically depend on the clinical stage of the disease and can include surgery, chemotherapy, radiotherapy, as well as combinations of these three. Radiotherapy can be divided into two main branches: brachytherapy (BT) and external beam radiation therapy. BT has been used with success for the treatment of cervical cancer. The treatment is achieved by placing radioisotopes on, in, or near the lesions of the tumor to be treated.[5,6] Several clinical studies have shown that the addition of BT after radical hysterectomy is a treatment option that offers the lowest recurrence rates for gynecological cancers, particularly in cases where residual cancer cells are suspected at the resection site.[5,7,8] In fact, the American Brachytherapy Society guidelines recommend implementing this post-operative strategy for close or positive tumor margins,

M. Kiseleva, T. Lescot, M.-A. Fortin
Département de Génie des Mines
de la Métallurgie et des Matériaux
Centre de Recherche sur les Matériaux Avancés (CERMA)
Université Laval
Québec G1V 0A6, Canada
E-mail: marc-andre.fortin@gmn.ulaval.ca

The ORCID identification number(s) for the author(s) of this article can be found under https://doi.org/10.1002/adhm.202300305

DOI: 10.1002/adhm.202300305

M. Kiseleva, T. Lescot, M.-A. Fortin
Laboratoire de Biomatériaux pour l'Imagerie Médicale
Axe Médecine Régénératrice
Centre de Recherche du CHU de Québec – Université Laval
Québec G1V 4G2, Canada

S. V. Selivanova
Faculty of Pharmacy
Université Laval
Québec G1V 0A6, Canada

S. V. Selivanova
Axe Oncologie
Centre de Recherche du CHU de Québec – Université Laval
Québec G1R 3S3, Canada

large or deeply invasive tumors, and cases presenting parametrial or vaginal involvement.[9] In such cases, BT can deliver a localized radiation dose to the resection site, demonstrating excellent local control of tumor progression together with low toxicity levels.[8]

The potential of gold nanoparticles (AuNPs) as additives to enhance the local radiation effect in BT, also referred to as radiosensitization, has been demonstrated for cervical cancer as well as for other types of cancers.[10–12] Radiosensitization agents are products that, when distributed in the cancer tissue surrounding a radioactive BT implant, increase the sensitivity of tumor tissue to radiotherapy. This strategy could allow a decrease in the activity needed per BT implant while limiting the total radiation dose delivered to the healthy tissues surrounding tumors.[13] Due to their high Z number (Z = 79), AuNPs irradiated by the low-energy photons emitted by BT implants produce secondary electron and photon emissions.[11,12,14,15] The biocompatibility of biomedical AuNPs for cancer applications has been reviewed in many publications.[16–19] Moreover, targeted drug delivery and drug loading capabilities and versatility of AuNPs make them a promising material for cancer therapy.[20,21]

Depending on the type of cancer, the delivery method of AuNPs for BT can vary greatly. Despite the promising benefits that AuNPs can offer as BT radiosensitizers, no efficient delivery system has been proposed to facilitate the administration of AuNPs to localized cervical cancer until now. Compared with many other types of organs treated by radiotherapy, the cervix is easily accessible through the vagina. Hence, therapeutic AuNPs can be administered topically at the cancerous tissue or the cervix surface immediately following resection surgery. Over the years, different devices have been developed to deliver therapeutics to the cervix: rings, gels, and cervical patches.[22–24] Among these various dosage forms, gels are known to be better tolerated by patients.[25] Therapeutic agents such as AuNPs can be loaded into hydrogels, and these formulations can then be used as localized delivery systems to improve therapeutic efficacy while reducing adverse effects on healthy tissues (compared with systemic administration).[23,26–29] Localized delivery approaches using hydrogels developed for cervical cancer treatment also provide an opportunity for personalized medicine. The therapeutic dose contained in hydrogel devices can be customized for each patient. The hydrogel's size and shape can also be adjusted according to the patient's needs with three-dimentional (3D) printing.

This article reports an original approach developed to accelerate the preclinical studies of AuNP-enhanced BT procedures, for which localized cervical cancer was selected as a case study. The approach combines the synergetic effects of BT, the radiosensitizing effect of AuNPs, and the flexibility of 3D-printed hydrogels and biomedical polymers. First, a biocompatible hydrogel formulation made of Pluronic F127 (PF127) and alginate, which we previously developed and reported for its mucoadhesive and NP-releasing properties,[30] was optimized as a matrix for the delivery of therapeutic AuNPs to cervical cancer. The in vitro characterization of the developed hydrogel formulation can be found in our previous work.[30] The formulation supplemented with AuNPs was studied for in vivo degradation in healthy BALB/c mice after subcutaneous (s.c.) injection by magnetic resonance imaging (MRI). The biocompatibility of the formulation was evaluated by measuring the local inflammation response of surrounding skin tissues by histological and immunofluorescence analyses. The general inflammation response was evaluated by measuring the level of inflammation proteins in the blood [IL-6, IL-10, monocyte chemoattractant protein-1 (MCP-1), IFN-γ, tumor necrosis factor (TNF), IL-12p70]. Then, the biodistribution of AuNPs released from the hydrogel was measured in vivo using nuclear imaging [positron emission tomography (PET), with ^{89}Zr-labeled AuNPs] and *ex vivo* by excising the organs and tissues of interest. Finally, the radiosensitization potential of AuNP-releasing hydrogels for brachytherapy treatments of cervical cancer was assessed by quantifying reactive oxygen species (ROS) in the tumor samples. For this, 3D-printed radioactive BT inserts were designed with a cushion of AuNP-containing hydrogel (**Figure 1**, panel a). Each device was fabricated by two successive 3D printing procedures. First, the cupola-shaped BT inserts were produced by additive manufacturing of polyether ether ketone (PEEK), a biocompatible and rigid polymer (Figure 1, panels b and c). Then, a radioactive ^{125}I seed, conventionally used for clinical BT procedures, was inserted in each implant. AuNP-hydrogel cushions were placed at the surface of these radioactive implants using a 3D printer (Figure 1, panel d).

The 3D printing approach allowed for adjusting the size and geometry of the BT inserts and AuNP-hydrogel cushions to each tumor inoculated in mice. These devices were placed in mice between the flank of the animal and the tumor by surgical insertion, radioactive face pointing toward the tumor and the skin (Figure 1, panel a). The degradation of the hydrogel and the tumor volume was monitored by MRI. The tumors were harvested on day 7 post-surgery, and the distribution of AuNPs and ROS was measured by histological analyses. This work describes an innovative approach to cervical cancer treatment, which brings together the advantages of BT, the radiosensitizing properties of AuNPs, customized local delivery by hydrogel and the convenience of 3D printing.

2. Experimental Section

2.1. Reagents and Chemicals

2.1.1. AuNP Synthesis

Deferoxamine mesylate salt (DFO, $C_{25}H_{48}N_6O_8{\cdot}CH_4O_3S$, 659.79 g mol^{-1}, ≥92.5%), dimethyl sulfoxide (DMSO, C_2H_6SO, ACS reagent, ≥99.9%), sodium borohydride ($NaBH_4$, 37.83 g mol^{-1}, 99.99% trace metal basis), and tetrachloroaurate ($HAuCl_4{\cdot}3H_2O$, 393.83 g mol^{-1}, ≥99.9% trace metal basis, 0.5 g mL^{-1} stock solution) were purchased from Millipore Sigma (Oakville, Canada). Thiol-polyethylene glycol-NHS (HS-PEG-NHS, 1000 Da, ≥95.0%) was obtained from Biochempeg Scientific Inc. (Watertown, USA). A cyanine amine dye (Cy5, $C_{38}H_{54}Cl_2N_4O$, 653.8 g mol^{-1}, 96%, excitation maximum 646 nm, emission maximum 662 nm, fluorescence quantum yield 0.2) with a terminal amine group was purchased from BroadPharm (San Diego, USA). Phosphate buffer saline (PBS) (pH 7.4) was purchased from Gibco by Life Technologies (Grand Island, USA).

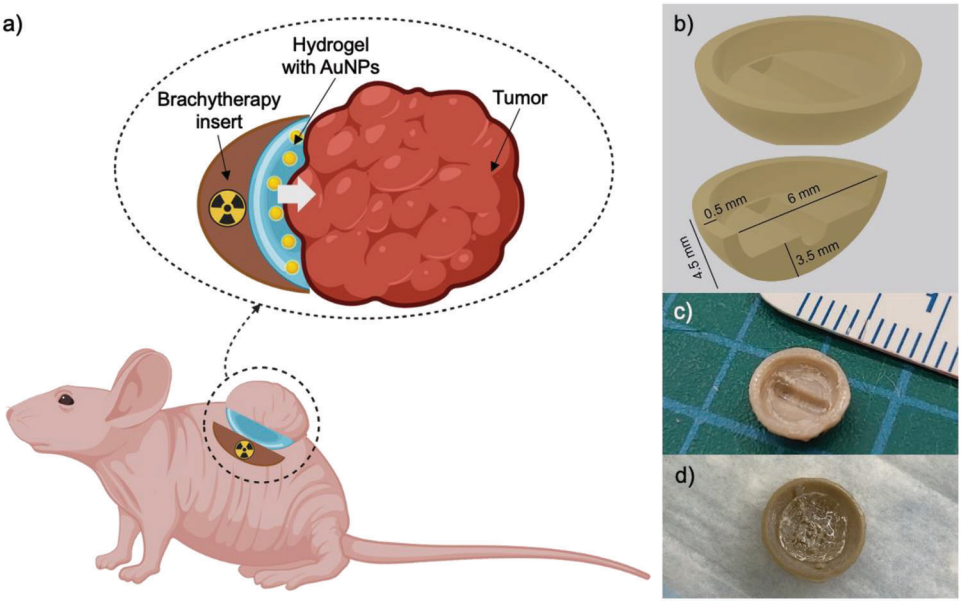

Figure 1. a) Schematic representation of the cupola-shaped 3D-printed radioactive BT inserts covered with a cushion of AuNP-containing hydrogel, specifically designed to facilitate preclinical BT studies (image created with BioRender.com). b) A 3D drawing of the implant with typical dimensions. c) Photograph of the 3D-printed and post-processed BT insert accommodating a radioactive ^{125}I seed prior to application of the AuNP-containing radiation-enhancing hydrogel layer. d) Photograph of the 3D-printed and post-processed BT insert with a hydrogel layer used for administration in the control group (without AuNPs).

2.1.2. Hydrogel Preparation

Pluronic F127 (PF127, 12 600 g mol^{-1}, suitable for cell culture), calcium chloride ($CaCl_2$, 110.98 g mol^{-1}, ≥93.0%), D-(+)-gluconic acid δ-lactone (GDL, $C_6H_{10}O_6$, 178.14 g mol^{-1}, ≥99.0%), and calcium carbonate ($CaCO_3$, 100.09 g mol^{-1}, ≥99.0%) were purchased from Millipore Sigma (Oakville, Canada). Ultrapure alginic acid sodium salt (Pronova SLG 100, sterile, medium viscosity 204 mPa s, with a guluronic acid content of 66%) was purchased from DuPont Nutrition & Biosciences, NovaMatrix (Sandvika, Norway).

2.1.3. Cell Culture

Normal human vaginal mucosa (CRL 2616) and human breast cancer (BT-474) cell lines were purchased from American Type Culture Collection (ATCC, USA). Human cervical cancer (HeLa) cells were kindly provided by the laboratory of René C. Gaudreault's and Sébastien Fortin (from Centre de Recherche du CHU de Québec – Université Laval). Fetal bovine serum, 0.5% Trypsin-EDTA (10X), penicillin (10 000 units mL^{-1}) – streptomycin (10 000 µg mL^{-1}), phosphate buffered saline 1X, Roswell Park Memorial Institute medium (RPMI 1640) supplemented with L-glutamine, keratinocyte-serum free media supplemented with human recombinant epidermal growth factor and bovine pituitary extract (BPE) were purchased from Gibco, Thermo Fisher Scientific (Canada). Dulbecco's Modified Eagle's Medium/Ham's Nutrient Mixture F12, Dulbecco's Modified Eagle's Medium (DMEM) with high glucose content, calcium chloride solution (0.5 M, suitable for cell culture), and insulin solution from bovine pancreas (1 mg mL^{-1}, in 25 mM HEPES, pH 8.2, suitable for cell culture) were obtained from Millipore Sigma (Oakville, Canada).

2.1.4. Animal Study

Radioactive iodine-125 seeds (^{125}I, 59.41 days half-life, 4.5 mm length, 0.5 mm diameter, 37.73 MBq (1.02 mCi) on November 3, 2021, Isoaid, Port Richey, USA) were kindly provided by Centre de Recherche du CHU de Québec – Université Laval (Nuclear Medicine division). BD CBA Mouse Inflammation Kit, BD Microtainer Capillary Blood Collector, and BD Microgard Closure (250–500 µL, additive – dipotassium EDTA), and polyethylene glycol (300 Da) were purchased from Fisher Scientific (Nepean, Canada). Lancets for blood collection (5 mm, Goldenrod) for blood collection were obtained from MEDIpoint Inc. (NY, USA). TWEEN 80 (1310 g mol^{-1}, suitable for cell culture) was purchased from Millipore Sigma (Oakville, Canada).

2.1.5. Histological Assessment

Rat IgG2a F4/80 (catalog #14-4801-82), anti-rat A488 (catalog #A-21208), and rat isotype IgG2a antibody (catalog #CBL605) were purchased from Thermo Fisher Scientific (Canada). Hoechst 33258 nuclear marker (catalog #B2883) was obtained from Millipore Sigma. Dihydroethidium (DHE, $C_{21}H_{21}N_3$, 315.41 g mol^{-1}, 96.9%) was purchased from MedChemExpress (NJ, USA). 3-morpholinopropane-1-sulfonic acid (MOPS), penicillin:gentamicin, Fungizone, bovine serum albumin, and optimal cutting temperature compound (OCT) were kindly provided by the laboratory of Julie Fradette and Dominique Mayrand (Centre LOEX – Université Laval).

2.2. Methods

2.2.1. Radiosensitizer Preparation: AuNPs Synthesis, Radiolabeling, and Cytotoxicity Assessment

Ultra-small AuNPs (core size of 5.6 nm ± 2.5 nm, hydrodynamic diameter of 18.5 nm ± 0.6 nm coated with a PEG-DFO organic layer were synthesized as previously described.[79]

To visualize the distribution of AuNPs in the tumor samples by fluorescence imaging, a near-infrared dye cyanine 5 amine (Cy5) was also attached to their surface (refer to Section S1, Supporting Information). A PEG molecule featuring a *N*-hydroxysuccinimide ending group (0.03 mmol, 2 mL, in PBS:DMSO mixture 25/75 v/v) was used to form a stable amide bond with DFO (0.09 mmol, 2 mL, in PBS:DMSO mixture 25/75 v/v) and Cy5 (1.5 µmol, 2 mL, in PBS:DMSO mixture 25/75 v/v). The reaction was carried out for 1.5 h at 4 °C. Then, this functionalized PEG molecule (PEG-DFO/Cy5) was presented to AuNPs following a previously described procedure.[79] For the PET imaging experiments, AuNPs were radiolabelled with zirconium-89 (^{89}Zr, [^{89}Zr]Zr-AuNPs), and the radiochelation stability was assessed (methodologies and results described in Section S2, Supporting Information). The tolerance of three (3) cell lines to these AuNPs was evaluated by cytotoxicity tests (cell viability and counting), as described in Section S3, Supporting Information.

2.2.2. Preparation of the PF127-Alginate Hydrogel for AuNP Release

PF127 powder was dissolved in HEPES buffer at 4 °C to avoid gelation and sterilized in an autoclave (121 °C, 45 min). Under aseptic conditions, sterile alginate powder was added to the PF127 solution to achieve the final concentrations of 20% w/v for PF127 and 0.5% w/v for alginate. Before beginning the experiments, this polymer solution (*PF-A*) was kept at 4 °C overnight. When required, AuNPs (AuNPs-PEG-DFO or AuNPs-PEG-DFO/Cy5; 0.2 µm filtered) were mixed with the stock polymer solution up to a final concentration of 0.1 mg Au mL^{-1} (based on the Au content, *PF-A + AuNPs* group). For the final part of the in vivo experiments (evaluation of the therapeutic effect of AuNPs), ultra-small iron oxide nanoparticles (USPIONs, a T_1-contrast agent for MRI described in Ref. [80]) were also mixed with the stock polymer solution to a final concentration of 1% v/v.

2.2.3. AuNP-Containing Hydrogel: In Vivo Degradation and Biocompatibility Study

In Vivo Degradation: MRI Study: All animal experiments were performed according to the guidelines of the Canadian Council on Animal Care (CCAC), and all procedures were approved by the local councils on animal care of Université Laval and the CHU de Québec Research Center (project # 2019—140, CHU-19-031).

The in vivo hydrogel degradation study was designed as shown in **Figure 2**, panel a. Two groups of mice (1-3-month-old healthy female BALB/c, Charles River, Montreal, Canada; $n = 6$ per group) were used in this experiment. On day 0, the mice were shaved on both flanks. Just before the injections, *PF-A* and *PF-A + AuNPs* solutions were treated with $CaCO_3$ (0.165 mol L^{-1}, 18 µL added to a 500 µL polymer solution and vortexed for 10 s) to initiate alginate cross-linking and gelation of the polymers. Then, freshly prepared D-(+)-gluconic acid δ-lactone (GDL, 0.33 mol L^{-1}, 18 µL) was added to each solution and vortexed for 10 s. Polymer solutions (200 µL) with (*PF-A + AuNPs*) or without (*PF-A*) AuNPs were injected in the right flank of the anesthetized animals (2% of isoflurane; oxygen flow of 0.5 L min^{-1}) using 23G × ¾in needles. Then, the formed hydrogels were visualized by MRI to measure their volumes (1 T M2M, Aspect Imaging, Netanya, Israel). The mice were placed in a 3.5 cm diameter RF coil and scanned using a T_1-weighted 2D spin echo sequence (field of view of 40 mm, 24 slices, 0.5 mm slice thickness, 0.1 mm slice gap, dwell time 25 µs, 320 × 320, fα 90°, echo time/repetition time (TE/TR) of 13.5/704.2 ms, 5 excitations, the overall duration of 18 min). After the scanning, the mice were injected in their left flank with Ringer's lactate solution (100–200 µL) at room temperature. MRI scans were repeated on days 3, 10, and 14. Obtained images were then analyzed with OsiriX Lite software (Pixmeo SARL, Switzerland), and regions of interest (ROIs) were drawn on each slice over the hydrogel areas. Hydrogel volumes were automatically calculated, which allowed for plotting the hydrogel degradation profiles.

Biocompatibility Study: Histological Assessment of the Surrounding Skin Tissues and Measurement of Local Inflammation Response around Hydrogel Implants: A MOPS solution supplemented with penicillin:gentamicin (50 000 U mL^{-1} and 12.5 mg mL^{-1}, respectively) and Fungizone 0.25 mg mL^{-1} was prepared by adding the antibiotics (1 mL) and Fungizone (1 mL) to MOPS solution (500 mL). Rat IgG2a F4/80 primary antibody's stock solution, anti-rat A488, and anti-rat secondary antibodies' stock solutions, as well as Hoechst 33258 nuclear marker's stock solution, were prepared at concentrations of 0.5 mg mL^{-1}, 0.2 mg mL^{-1}, 0.2 mg mL^{-1} and 50 µg mL^{-1}, respectively. Rat isotype IgG2a antibody was used for isotypic controls (0.1 mg mL^{-1} stock solution, 1/40 dilution for cryosections).

Hydrogel Excision from the Animals: On day 14 after injection, the hydrogels were excised with the surrounding tissue to prepare histological specimens. The skin from the opposite flank was used as a negative control. The skin of infected CD-1 mice (kindly provided by the laboratory of Julie Fradette, Centre LOEX – Université Laval) was used as a positive control. All incubations were carried out at room temperature unless specified otherwise.

Pre-Processing of Histological Specimens: The tissues were placed in histological cassettes containing a MOPS: 3.7% formalin solution and incubated for 1–2 h, followed by a 1.5-h incubation in a MOPS: 1% bovine serum albumin solution. Then, the tissues were cut into two pieces using a surgical scalpel (#4, blade #22), as shown in Figure S6, Supporting Information, and processed in two ways: inclusion in paraffin for H&E staining and inclusion in OCT for immunofluorescence staining.[81]

Inclusion of Histological Specimens in Paraffin and H&E Staining: The samples were kept in 2 mL of Bouin's solution overnight. The fixed tissues were then placed in the histology cassettes and incubated sequentially in a formalin (3.7%): EtOH (10:90 v/v) solution for 30 min, an EtOH:H_2O_D (50:50 v/v) solution for 30 min, an EtOH:H_2O_D (75:25 v/v) solution for 30 min, 100% EtOH for 1 h, and twice in 100% xylene for 30 min. The cassettes were then transferred to preheated paraffin (56 °C), incubated for 2 h, cut (50 µm thickness), stained with H&E, and imaged by an optical

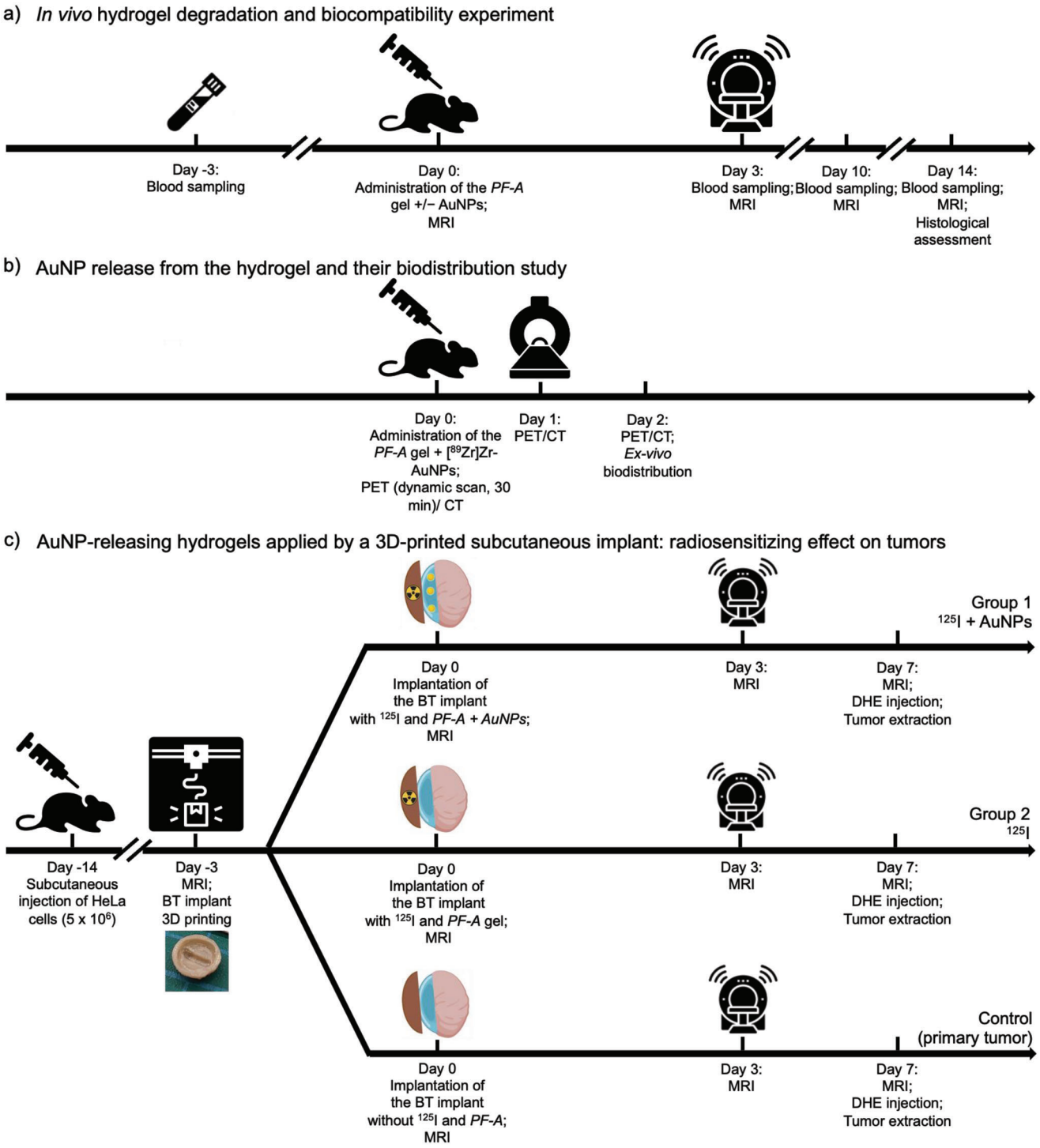

Figure 2. Design of the in vivo experiments: a) timeline of the in vivo hydrogel degradation (by MRI) and biocompatibility experiment; b) timeline of the [^{89}Zr]Zr-AuNPs hydrogel release and biodistribution study (by PET); and c) timeline of the study to demonstrate the radiosensitizing effect on xenograft tumors, of AuNP-releasing hydrogels applied by a 3D-printed subcutaneous implant.

microscope (Axio Imager M2, 10× lens, exposure time 4 ms, 14% brightness).

Inclusion of Histological Specimens in OCT and Immunofluorescence Staining: The samples were incubated in an OCT:$CaCl_2$ (0.05 mol L^{-1}) (50:50 v/v) solution for 2 h and in 100% OCT for 30 min. The tissues were then transferred to OCT-containing custom-made aluminum cassettes for a 30-min incubation, followed by a 30-min freezing step (−80 °C in a freezer). The tissues were sliced with a cryostat (20 µm sections). These cryosections were then stained by overnight incubation in a MOPS solution (350 µL) supplemented with penicillin:gentamicin and Fungizone and containing Rat IgG2a F4/80 primary antibody (1/200 dilution). This step was followed by overnight incubation in MOPS solution (350 µL) supplemented with penicillin:gentamicin and Fungizone and containing anti-rat A488 (1/200 dilution) secondary antibody and the Hoechst 33258 nuclear marker (1/100 dilution). After each incubation, the tissues were washed three times with MOPS solution (500 µL) supplemented with penicillin:gentamicin and Fungizone and imaged by a confocal microscope (LSM 700, Zen 2010 software by Zeiss).

General Inflammation Response by Blood Collection and Cytokine Detection: Three days before the hydrogel injection (day -3), then on days 3, 10 and 14, blood samples were collected from the mandibular vein of unanesthetized animals with 5-mm lancets into EDTA-coated collection tubes. Right after blood collection, the animals were injected with Ringer's lactate solution (s.c.; 3× the extracted blood volume). Blood plasma was separated by double centrifugation (3200 g, 10 min, 4 °C). Inflammatory response proteins such as Interleukin-6 (IL-6), Interleukin-10 (IL-10), MCP-1, Interferon-γ (IFN-γ), TNF, and Interleukin-12p70 (IL-12p70) protein levels were quantified using Cytometric Bead Array Mouse Inflammation Kit from BD Biosciences. First, a calibration curve was plotted using mouse inflammation standards provided with the kit. The recommended protocol was followed at half volume. Samples were processed on a flow cytometer BD FACSCanto II and analyzed using the FCAP Array Software (version 3.0). The results are presented along with a calibration curve for each cytokine in Figure S9, Supporting Information.

2.2.4. AuNP Release from the Hydrogel and Their Biodistribution Study by PET

AuNP Radiolabeling: [^{89}Zr]Zr-chloride (58.1 MBq) in hydrochloric acid (1 mol L^{-1}, 63 µL) was neutralized with Na_2CO_3 (1 mol L^{-1}, 30 µL) to pH 7.0 and diluted with HEPES buffer (100 mmol L^{-1}, 107 µL). AuNPs grafted with DFO (AuNPs-PEG-DFO) and suspended in HEPES buffer (0.935 mg mL^{-1}, 0.35 mL) were added to the radioisotope solution. The chelation reaction of ^{89}Zr with DFO was allowed to proceed at ambient temperature for 1 h. The radiolabeling efficiency was measured using thin-layer chromatography (TLC) as described in Section S2, Supporting Information. The radiolabeled AuNPs, [^{89}Zr]Zr-AuNPs, were then mixed with sterilized PF127-alginate polymer solution at 4 °C. The final concentrations of PF127, alginate and [^{89}Zr]Zr-AuNPs in the polymer solution were 20% w/v, 0.5% w/v and 0.1 mg mL^{-1}, respectively.

PET/CT Imaging: The experimental design is shown in Figure 2, panel b. PET imaging was performed using a LabPET II scanner (IR&T, Sherbrooke, Canada). A group of BALB/c mice ($n = 6$) was anesthetized with isoflurane (induction chamber, 3% of isoflurane, oxygen flow of 1 L min^{-1}) and transferred to the scanner mouse bed with an integrated nose cone (2% of isoflurane, oxygen flow of 0.5 L min^{-1}). The mice were s.c. injected with the PF127-alginate polymer solution (150–200 µL) containing [^{89}Zr]Zr-AuNPs (3–4 MBq per injection). Within 5 min after injection, dynamic scans were acquired for 30 min. Static whole-body scans (acquisition time of 1 h) were performed on days 1 and 2 p.i. At the end of each acquisition, the data were reconstructed (20 iterations) and corrected for radioactivity decay and random events (no dead time, attenuation, or scatter correction applied). For the analysis of subsequent scans, the doses were corrected for radioactive decay, referring to the time of the first PET acquisition for each animal. Values for the average radioactivity concentration in selected organs were obtained by drawing ROIs over each organ of interest with the VivoQuant 3.5 software. The values in cps mL^{-1} were converted to kBq g^{-1} using the calibration factor between the PET scanner and the dose calibrator, assuming a tissue density of 1 g mL^{-1}; the values were then divided by the total administered radioactivity to obtain the image-derived percentage administered radioactivity per gram of tissue (% ID g^{-1}). After each PET scan, whole-body CT imaging was performed to provide an anatomical reference. For this, the eXplore Locus micro-CT scanner system (GE Healthcare; 40 kV, 450 µA, effective pixel size 0.089 µm) was used. At the end of each acquisition, the data were reconstructed, and calibration in Hounsfield units was performed using standards of air, water and bone co-scanned with each mouse.

Ex Vivo Biodistribution Study: After the last scan, the mice were euthanized by intracardiac exsanguination. Organs of interest were extracted, weighed, and their radioactivity was measured in a gamma counter (Perkin Elmer). Values were corrected for the radioactive decay and expressed as % ID g^{-1} (mean ± SD). To correlate the radioactivity values with the concentration of Au in organs, after the radioactivity decayed, the pre-weighted residual gel, urine and kidneys were completely lysed in 2 mL of fresh aqua regia. The acid was left to react with the specimens in screw-capped DigiTubes for one week. After that, the samples were sonicated for 20 min and centrifuged (1000 g; 5 min) to remove the precipitate. Then, the supernatant was heated using an oil bath at 80 °C for 2 h, followed by the addition of H_2O_2 (1 mL) at 80 °C and evaporation of the solvent to 1 mL. The Au content in each sample was measured by microwave plasma atomic emission spectrometry (MP-AES, Analyst 800 model, PerkinElmer).

2.2.5. AuNP-Releasing Hydrogel Applied as a 3D-Printed Subcutaneous Implant: Radiosensitizing Effect on Tumors

The last step of this study consisted in measuring the radiosensitizing effect of the AuNP-eluting hydrogel distributed in the vicinity of a radioactive brachytherapy implant on cervical cancer tumors (Figure 2, panel c). This experiment was achieved by developing by 3D printing of a brachytherapy implant optimized for dispensing AuNP-releasing hydrogels in the mouse model (see Figure 1).

Fabrication of a 3D-Printed Radioactive Brachytherapy Insert for Surgical Implantation in the Mouse Model: Supports for ^{125}I

radioactive seeds ("*brachytherapy inserts*"), also used to apply the AuNP-eluting hydrogel at the surface of xenograft tumors, were 3D-printed from polyetheretherketone (PEEK). Computer-aided design (CAD) models of the inserts were drawn as small cupolas of the dimensions displayed in Figure 2, panel b. The CAD model was converted into .stl files (CREO Parametric 6.0, student edition, Boston, USA) that were then imported into a slicing software (Simplyfy3D, Version: 4.1.2, Simplify3D Inc., Ohio, USA) to generate g-code files. The implants were printed using a PEEK FFF printer (P220, Apium Additive Technologies GmbH, Karlsruhe, Germany). Prior to printing, the PEEK filaments (medical grade; 450 Natural; 1.75 mm diameter; Apium Additive technologies GmbH, Karlsruhe, Germany) were dried at 80 °C for 3 h using a filament drier (FD1, Apium Additive Technologies GmbH, Karlsruhe, Germany). A fixative (DimaFix, DIMA 3D, Valladolid, Spain) was applied to the print bed to ensure adhesion of the first layer during the process. A 0.2 mm diameter printing nozzle was used for a layer thickness of 0.1 mm, a nozzle temperature was set to 485 °C, and a print bed temperature was set to 130 °C. Throughout the printing process, the filament was kept at a temperature of 60 °C. No infill was programmed in the printing process. At the post-processing step, the brim was removed by cutting it off with a surgical blade (#1 with blade #11; X-ACTO, USA); the printing support located in the convex part of each insert was removed by shear cutters (1 mm, model 170, PLATO, Techspray, USA). The remaining support material in the convex part was removed by the rotary drill (Stylo 1050, Dremel) with grinder bits. The inserts were sandblasted with sanding pads (2″ × 2″ aluminum oxide abrasive; McMaster-Carr, from 400 grit up to 12 000 grit; 4 min for each step). Notches were machined in the inner part of each insert to accommodate one (1) brachytherapy seed (^{125}I; 0.75–0.89 mCi at the time of the experiment). The inserts were then rinsed with nanopore water and disinfected with ethanol.

Printing of Lens-Shaped AuNP-Containing Hydrogel Cushions for Application on the Brachytherapy Insert: The 3D-printed PEEK BT inserts were lined with a 3D-printed cushion of AuNP-releasing hydrogel. For this, a numeric model for the hydrogel shape was designed using the FreeCAD software (0.19.2, OpenCasCade project, Germany). Hydrogel structures were 3D-printed using a UV-sterilized CELLINK Bio X extrusion-based system. Hydrogel polymer solutions supplemented with AuNPs-PEG-DFO/Cy5 and USPIONs (see description in Methods, Section 2.2.2) were placed in a 3 mL syringe printhead of the printer. A plastic nozzle with an inner diameter of 0.2 mm was used for the extrusion. The printhead was then heated up to 37 °C, which resulted in the rapid gelation of the PF127 component and the formation of a soft gel. Lens-shaped hydrogel cushions (typical dimensions: Ø 6 mm, h = 1.5 mm) were printed in Petri dishes placed on the preheated (37 °C) printer bed. Extrusion was performed at a rate of 8 mm s^{-1} under an applied pressure of 42 kPa. After printing, the soft gel structures were stabilized via ionic cross-linking of alginate chains (10 min immersion in a 0.1 mol L^{-1} aqueous solution of $CaCl_2$) and then rinsed in deionized water.

Tumor Inoculation in the Mouse Model: Tumor xenografts (referred to as primary and secondary tumors) were prepared by injecting HeLa cells (5 × 10^6 cells) s.c. in both flanks of nu/nu mice (n = 24, 1-3-month-old female nu/nu, Charles River, Montreal, Canada), and the body weight of the mice was measured three times a week. The tumors were allowed to grow to 4–5 mm (as measured by caliper), and then, on day -3 (baseline), precise tumor volume was determined using MRI imaging (see details below). From that point, the animals were randomized into three groups (n = 6 each). In the first experimental group ("I-125 + AuNPs"), the animals received a radioactive BT insert (^{125}I, 0.75–0.89 mCi) lined with a lens-shaped USPION-containing *PF-A + AuNPs* hydrogel cushion (see details of the surgery in the section below). The animals of the second experimental group ("I-125") received a radioactive BT insert lined with a lens-shaped USPION-containing *PF-A* hydrogel cushion (without AuNPs). Finally, the last group of animals, the control group, received a non-radioactive BT insert lined with a lens-shaped USPION-containing *PF-A* hydrogel cushion (without AuNPs). Moreover, the secondary tumors developed on the other flank of mice were not exposed to the surgery or any treatment, but their volume was monitored.

Aseptic Surgery for Implant Insertion: BT seeds conventionally used for prostate and eye cancer brachytherapy were glued in the notch of the 3D-printed PEEK inserts (Figure 1, panel c). The 3D-printed lens-shaped AuNP and USPION-containing hydrogel cushions were placed on the inner surface of the BT insert on top of the radioactive seed. These implants were placed s.c. on the xenograft tumors by surgery in a biological hood under aseptic conditions. To keep the animal warm, a heating pad (Deltaphase Isothermal Pad) was used throughout the surgery. Analgesia was provided s.c. (buprenorphine 0.05 mg kg^{-1} for pre-op, carprofen 20 mg kg^{-1} for post-op, lidocaine-bupivacaine 0.05 mL for local analgesia). Anesthesia was provided with isoflurane (3% isoflurane inhalant in an induction chamber; oxygen flow of 1 L min^{-1}) until deep sedation was established. Then, isoflurane was reduced to 2% for the surgery (oxygen flow of 0.5 L min^{-1}). Lidocaine-bupivacaine was injected along the incision site. Approximately 1 cm^2 of dorsal skin adjacent to the tumor was aseptically prepared by three alternating scrubs of chlorhexidine 0.5%. The animals were kept hydrated by s.c. injection of Ringer's lactate solution (0.1 mL hourly). Sterile drapes were placed to outline the surgical approach site on the animals. Incisions of 8–10 mm were performed adjacent to the tumor. Forceps were used to lift the skin from the lumbosacral region, and a pair of scissors was used for the skin incision. Another pair of sterile forceps was used to create a 1-cm s.c. cavity around the tumor, followed by the insertion of the brachytherapy implants in these cavities with the hydrogel cushion facing the tumor. The incision was then closed using Vicryl 5–0 sutures. The animals were transferred to clean cages, placed on a heating pad, and continuously monitored until complete wake-up.

In Vivo MRI Tumor and Hydrogel Follow-Up: Three days before the surgery, just after the surgery, and on days 3 and 7 after the implantation, the mice were MRI-scanned to monitor the position of the implants, the residual volume of hydrogel and the volume of the tumors. The scanning procedure described in Section 2.2.3 was used, except that a slice thickness of 0.5 mm, a dwell time of 16 µs, a matrix of 280 × 280 25 µs, echo time/repetition times (TE/TR) of 11/480 ms and 6 excitations were programmed, for a total duration of 13 min 26 s. After scanning, mice were injected s.c. with Ringer's lactate solution (100 µL). The MR images were analyzed by the OsiriX Lite software (Pixmeo SARL, Switzerland). ROIs were drawn over the contours of the tumors and of

the hydrogel cushions. Tumor and hydrogel volumes were then computed automatically, and their volumes were calculated.

Visualization of Reactive Oxygen Species (ROS) Generated by the Radiosensitizers at the Tumor: Dihydroethidium (DHE) was used as a histological probe to visualize the presence of ROS generated at the tumor site by AuNPs irradiated by the brachytherapy implants.[43,44] DHE was dissolved in saline with DMSO, PEG 300, and Tween 80 in a 45:10:40:5 proportion (v/v/v/v) and according to the instructions of the manufacturer. The solution was injected intratumorally (0.1 mg kg^{-1}, 50 µL; syringe without dead volume, 1705 RN, Hamilton, Reno, USA; fitted with a 30-gauge needle) 30 min before euthanasia of the animals, using a stereotaxic instrument (model 963, Kopf Instruments, Tujunga, USA). The solution was injected at a flow rate of 5 µL min^{-1} with a UMPII micropump (World precession Precision Instruments, Saratoga, USA). The animals were kept anesthetized throughout the procedure. The tumors were extracted using a surgical kit and preserved in OCT (for detection of ROS and AuNPs-PEG-DFO/Cy5). A cryostat was used to slice 20 µm sections that were imaged by a confocal microscope (LSM 700, Zen 2010 software by Zeiss).

Monte Carlo Simulations of the Absorbed Dose and Photon Fluence in the Tumor Tissue from the ^{125}I Seed: The Monte Carlo simulations were conducted to calculate the absorbed radiation dose and photon fluence along the tumor depth from the photons emitted by a ^{125}I seed. The calculations were performed using the TOol for PArticle Simulation (TOPAS) Monte Carlo code,[82,83] version 3.8, released in July 2022. The simulation setup consisted of three geometries: a model of the ^{125}I seed (OncoSeed Model 6711), a rectangular representation of a PEEK brachytherapy insert, and a cubical box filled with tumor tissue, with the seed being situated between the first two geometries. The ^{125}I seed was simulated according to the methodology reported by Poher et al.,[84] and the photon spectrum emitted from the seed was adapted from Rivard et al.[85] The PEEK rectangular sheet, with dimensions of 6.0 × 6.0 × 1.0 mm, was composed of three elements: C at 79.15%, H at 4.19%, and O at 16.64%.[86] The 6.0 × 6.0 × 6.0 mm cubical box filled with tumor tissue was composed of 9 elements H (64.32%), C (4.78%), N (1.06%), O (29.64%), Na (0.05%), P (0.04), S (0.04%), Cl (0.03%), and K (0.03%).[87]

The simulations took ≈9 h to complete, and the results were recorded in a 3D matrix divided into 20 × 20 × 20 voxels with a voxel size of 0.3 × 0.3 × 0.3 mm. The statistical uncertainty was less than 1%. The simulations were executed on a high-performance computing cluster provided by Compute Canada, utilizing a single node featuring a 40-core Intel Gold 6148 Skylake 2.4 GHz processor. The physics parameters used in the simulation included the G4em-Livermore physics list, CutForElectrons of 0.5 mm, CutForGamma of 1.0 cm, Auger, Particle-induced X-ray emission, and AugerCascade enabled. The dose distribution and photon fluence along the central axis of the tumor matrix were extracted from the 3D grids using Python scripts (NumPy library).

Statistical Analysis: For Section 2.1.1 (in vivo degradation of hydrogels), the statistical differences between the two groups were analyzed according to the paired Student's *t*-test. Statistical significance was presented when the *p*-value was less than 0.05 (*) and less than 0.005 (**). The data is given as mean ± standard deviation ($n = 6$). For Section 2.3 (AuNP-releasing hydrogels applied as a 3D-printed subcutaneous implant, **Figure 3**), the data were analyzed using the one-way ANOVA test ($p < 0.05$) followed by the post hoc Tukey HSD test and are presented as mean ± SD, $n = 5$.

3. Results

3.1. AuNP-Containing Hydrogel: In Vivo Degradation and Biocompatibility Study

3.1.1. In Vivo Degradation of Hydrogels

In this study, MRI was used to monitor in vivo the degradation of PF127-alginate hydrogels with (*PF-A + AuNPs*) and without (*PF-A*) the addition of AuNPs. MRI is a non-invasive imaging modality based on the detection of ^{1}H protons. Therefore, it is commonly used for the in vivo visualization of hydrogels and evaluation of their degradation over time.[31–34] The experimental design of this study is shown in Figure 2, panel a. For the injections, the *PF-A + AuNPs* and *PF-A* samples were pre-cross-linked using $CaCO_3$ and D-(+)-gluconic acid δ-lactone (GDL). Compared to $CaCl_2$ and $CaSO_4$, $CaCO_3$ has very low solubility in aqueous media at physiological pH. This allows a more uniform distribution of the bivalent Ca^{2+} ions that induce the cross-linking of alginate in the polymer solution before gelation occurs. After adding GDL, complete gelation occurred in about 3 min, providing enough time to fill a syringe for s.c. injections. A few seconds after each injection, an elliptical lump was observed under the skin of mice, thereby confirming the gelation of hydrogels. Although the PF127-alginate hydrogels (PF-A + AuNPs and PF-A) were administrated without the addition of any MRI-contrast agent, they appeared delineated by the subcutaneous fat and were distinctly visualized on the scans over the course of the 14-day study (**Figure 4**, panel a; white arrows).

As expected, the MRI scans revealed a two-step evolution in hydrogel degradation, similar to what was observed in our preliminary experiments with PF127-alginate formulations.[30] In both experimental groups (*PF-A + AuNPs* and *PF-A*), similar degradation profiles were obtained (Figure 4, panel b). The initial steep decrease is attributed to the rapid diffusion of the PF127 component out of the polymer network, which is due to its low mechanical properties and fast dissolution rate.[35] While PF127 diffuses away creating microscopic pores in the hydrogel network—confirmed by SEM analysis of the degraded samples in Ref. [30]—the Ca^{2+}-cross-linked alginate component remains in the hydrogel's structure. In the second step of the degradation process, the alginate network begins its slow disintegration by releasing chelated Ca^{2+} ions. The results of SEM hydrogel analysis can be found in Ref. [30] (including in the Supporting Information section of Ref. [30]), whereas the results of the TGA characterization study for the measurement of PF127 and alginate content in the hydrogel can be found in the Supporting Information section.

On day 3 after hydrogel administration, the remaining volumes of *PF-A* and *PF-A + AuNPs* were 44% and 37%, respectively (no statistically significant difference between the two groups). On day 14, these values were 26.1 ± 2.8% and 20.6 ± 3.0% for *PF-A* and *PF-A + AuNPs* groups, respectively. The difference between these values was statistically significant and could be attributed to the presence of AuNPs in the latter group. AuNPs

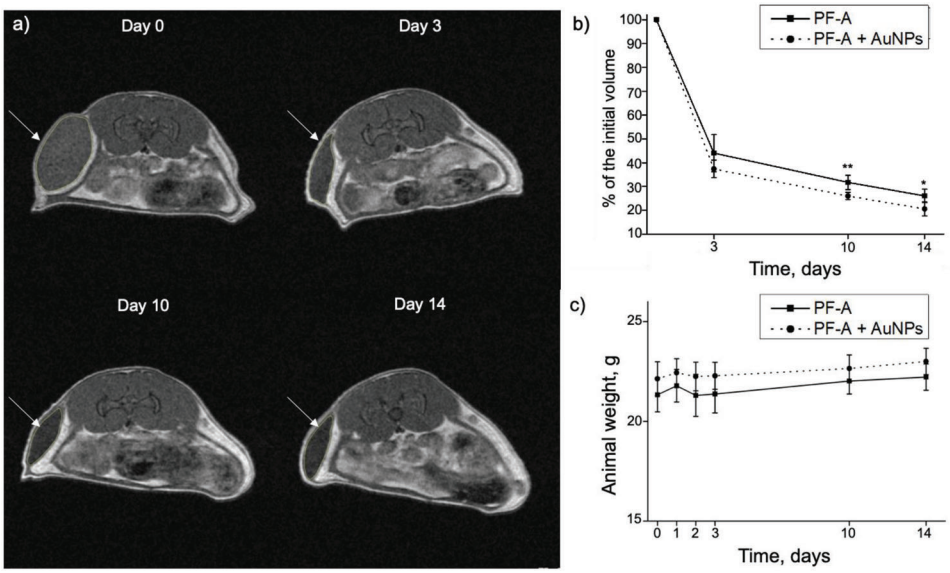

Figure 3. Visualization of BT inserts, tumors, and hydrogel cushions with MRI. a) Representative MRI images of mice from the ^{125}I + AuNPs group, 3 days before, right after, and 7 days post-surgery (the tumors are pointed with white arrows). b) Hydrogel volume ($n = 5$) and c) tumor volume ($n = 5$) quantified with MRI. The I-125 + AuNPs group received a radioactive BT insert lined with a lens-shaped USPION-containing *PF-A + AuNPs* hydrogel cushion, while the I-125 group received a radioactive BT insert lined with a lens-shaped USPION-containing *PF-A* hydrogel cushion (without AuNPs). The control (primary tumor) group was also exposed to the surgery and had a non-radioactive BT insert lined with a lens-shaped USPION-containing *PF-A* hydrogel cushion (without AuNPs). The secondary tumors developed on the other flank of the same mice were not exposed to the surgery but were used as an additional control (secondary tumor, no surgery). The data were analyzed using the one-way ANOVA test ($p < 0.05$) followed by the Post Hoc Tukey HSD test and are presented as mean ± SD, $p < 0.05$ (*).

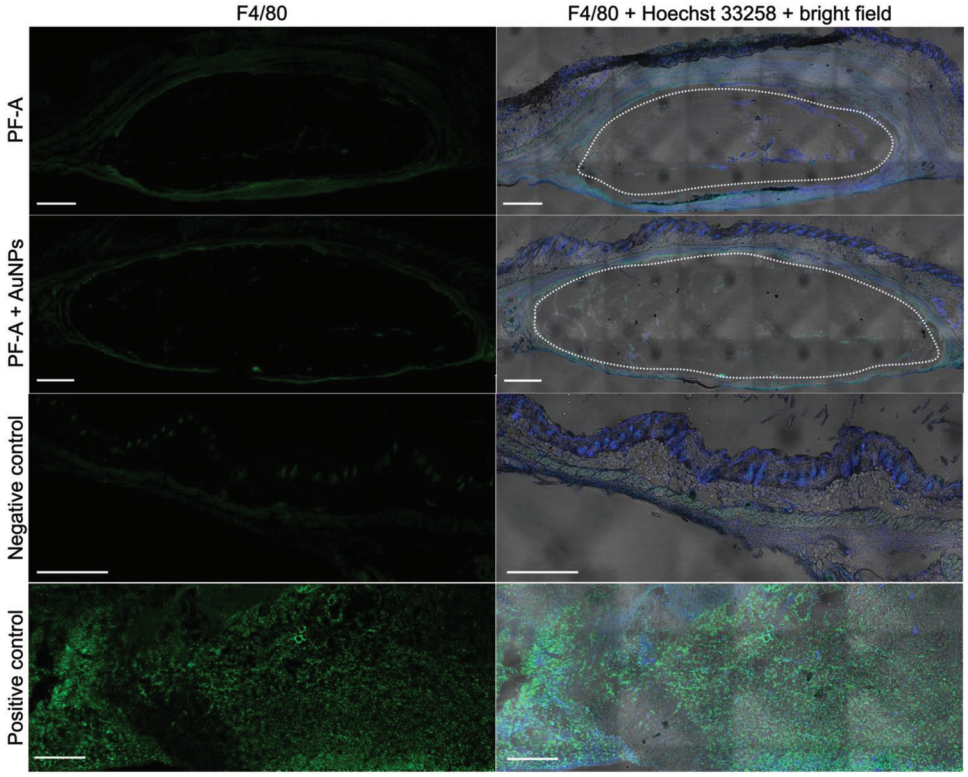

Figure 4. Results of the in vivo degradation study of AuNP-containing hydrogels (*PF-A + AuNPs* and *PF-A* formulations). a) MRI scans of the mouse injected with *PF-A + AuNPs*: white arrows indicate the hydrogel lumps. b) In vivo degradation profile of the two formulations (*PF-A + AuNPs* and *PF-A*), $n = 6$, paired Student's *t*-test, $p < 0.05$ (*) and < 0.005 (**). c) No change was noted in the body weight of mice over a 14-day course, $n = 6$. The data are presented as mean ± SD.

that diffuse out of the hydrogel network during the degradation process, particularly after the majority of PF127 is eliminated, could create nano-channels and pores in the polymer network. This could expose the interior of the hydrogels to biological fluids and facilitate the leaching of Ca^{2+} ions with a loosening effect on the remaining alginate network.

The body weight of mice was continuously monitored up to day 14 (Figure 4, panel c), and no side effects such as appetite loss, behavioral change, dehydration or body weight loss were observed.

3.1.2. Biocompatibility Study: Histological Assessment of the Surrounding Skin Tissues and Measurement of Local Inflammation Response around hydrogel Implants

Upon administration of hydrogels, the body's immune system is susceptible to recognizing such implants as foreign, which would be a natural mammalian protection mechanism.[36,37] This mechanism can be divided into several steps. First, proteins adsorb in a non-specific manner on the components of the hydrogel network. Then, macrophages infiltrate the network, recognize the adsorbed proteins, and phagocytize both proteins and hydrogel components to which they are attached. Finally, macrophages fuse to form foreign-body giant cells that secrete cytokines. These cytokines, in turn, induce fibroblasts to deposit a dense, avascular layer of collagen on the implant. If triggered and fully activated, this mechanism can lead to the formation of a capsule impermeable to most molecules in the surrounding microenvironment.[36,38] This process can cause tissue distortion and pain.[38] Therefore, this process must be avoided in a functional hydrogel formulation specifically designed to allow the release of AuNPs. Because macrophages are the key drivers of the foreign-body reaction (step 2),[38] their presence in the tissues around the hydrogel implants was evaluated using histology. Animals were sacrificed on day 14 after hydrogel administration, and the tissues were prepared and sliced (20 µm-thick) for immunofluorescence and reacted with a pan-macrophage marker F4/80 (green).

The images from this histological assessment are presented in **Figure 5**. First, the cavities left by the soft hydrogels were visible in the slides (white ovals). Only slight evidence of cellular invasion (blue signal) was detected at the surface of the implants, and a few macrophages (green signal) were found at the periphery of hydrogel implants for both experimental groups (*PF-A* and *PF-A + AuNPs*). The level of green signal found for the hydrogel samples was close to that of negative controls. By comparison, the positive control showed a very high green signal, about ten and four times higher than for the *PF-A* and *PF-A + AuNPs* groups, respectively. Overall, these results indicate a mild local inflammation response.

Inflammation of the skin surrounding the implant was also visualized by histological coloration using hematoxylin-eosin (H&E) staining (cell nuclei – blue; cytoplasm, elastin, and collagen – pink). These samples were particularly challenging to process due to the softness of alginate. **Figure 6** is a representative collection of H&E-stained images for each group.

The H&E-stained images revealed a certain fragmentation of the hydrogel volumes after 14 days of implantation in the animals. Some inflammatory cells were present at the surface of the gel volumes, as pointed out by solid arrows in Figure 6, panels a and b, which correlates well with the results indicated by immunofluorescence results (Figure 5).

Interestingly, there were more inflammatory cells around detached hydrogel fragments in areas showing evidence of resorption of the scaffolds by the host tissue. Moreover, more inflammatory cells could be seen in the surrounding conjunctive tissue in both *PF-A* and *PF-A + AuNPs* groups compared to the control one, which is also a sign of the developed mild inflammation response. However, the H&E staining provided no clear indication of the collagen capsule formation around the implants since the thickness of the conjunctive tissue surrounding them is comparable to that observed for the control sample. Therefore, no apparent fibrotic response was developed due to the implant administration in mice.

3.1.3. General Inflammation Response by Blood Collection and Cytokine Detection

The general inflammation response was evaluated in the mouse model by quantifying the expression of both pro-inflammatory (IL-6, MCP-1, IFN-γ, TNF, IL-12p70) and anti-inflammatory (IL-10) cytokines in the blood (Figure S9, Supporting Information). For the *PF-A* group, only trace amounts of IL-6, IFN-γ, TNF, IL-12p70, and IL-10 cytokines were detected at each time point (all below the standard range of quantification). Only the MCP-1 level appeared to fall in the standard range; however, very close to the lower quantification limit. Its level peaked at day 3 (36.8 ± 21.5 pg mL^{-1}), then returned to baseline values (19.2 ± 6.2 pg mL^{-1}). However, even the highest concentration of MCP-1 measured on day 3 was found to be within the normal range for immunocompetent BALB/c mice in a non-inflamed state.[39] For comparison, in other studies reporting results for mice infected with a TcI strain of *Trypanosoma*, the blood concentration of this cytokine after 8 days was >100 pg mL^{-1}.[39] For the *PF-A +AuNPs* group, the MCP-1 level demonstrated the same trend, peaking at day 3 (46.2 ± 14.2 pg mL^{-1}) and then decreasing to baseline values. The concentration of IL-6, IL-10, and IFN-γ cytokines was below the standard quantification range for all time points. Interestingly, for this group, the expression of TNF (20.0 ± 32.8 pg mL^{-1}) and IL-12p70 (49.4 ± 79.0 pg mL^{-1}) appeared higher at day 10. A closer look reveals that only one mouse from that group developed an elevated concentration of these cytokines at one time point, which was considered an outlier. The levels of TNF and IL-12p70 returned to the baseline values by day 14 and were equal to 7.2 ± 6.5 and 12.8 ± 18.0 pg mL^{-1}, respectively. Considering cytokine level expressions in the mouse model, the injection of *PF-A* and *PF-A + AuNPs* groups in the flank of mice did not trigger an immune response.

3.2. AuNP Release from the Hydrogel and Their Biodistribution Study by PET

The release of AuNPs radiolabeled with ^{89}Zr ([^{89}Zr]Zr-AuNPs) from the *PF-A* hydrogel was investigated in vivo with PET. The timeline of these experiments is shown in Figure 2, panel b. A first dynamic PET scan was performed right after the s.c. injection of the gels and lasted for 30 min, while static scans followed

Figure 5. Histological assessment of the skin tissues surrounding the hydrogel implants (local inflammation response) 14 days after administration. Results are presented for both *PF-A* and *PF-A + AuNPs* groups. Cell nuclei are stained in blue (Hoechst 33258); macrophages are stained in green (F4/80 marker). The skin of CD-1-infected mice was used as a positive control, whereas the skin from the opposite flank of the experimental mice was used as a negative control. White ovals mark the cavities left by the fragile hydrogel volumes. The right side is a superposition of blue and green fluorescent signals on bright field optical microscopy [note: mosaics were reconstituted with several bright field images, which left geometrical patterns in the process (image artifact)]. The thickness of each slice was 20 µm, and the scale bar is 500 µm.

on days 1 (24 h +/− 2 h) and 2 (48 h +/− 2 h) after the injection. Each PET scan in this study was complemented by a CT scan for anatomical reference. The PET/CT study results are presented in **Figure 7**, panels a–c.

At 30 min after s.c. injection, the signal from [^{89}Zr]Zr-AuNPs particles was mainly found in the volumes corresponding to hydrogel in the flanks of the mice (coronal view in Figure 7, panel a). Interestingly, as soon as 5 min after the injection, some activity was detected in the bladder (sagittal and transverse views in Figure 7, panel a), indicating an early elimination of [^{89}Zr]Zr-AuNPs from the body. Activity in the bladder built up to 22.96 ± 5.30% ID g^{-1} in the first 30 min (Figure S10, Supporting Information), which confirms that these ultra-small AuNPs found their way through the vascular system and were eliminated by renal clearance. The presence of [^{89}Zr]Zr-AuNPs in the bladder at this early time point can be attributed to one of the drawbacks of the in situ polymer gelation, which is not an instantaneous process. Depending on the composition of the formulation and

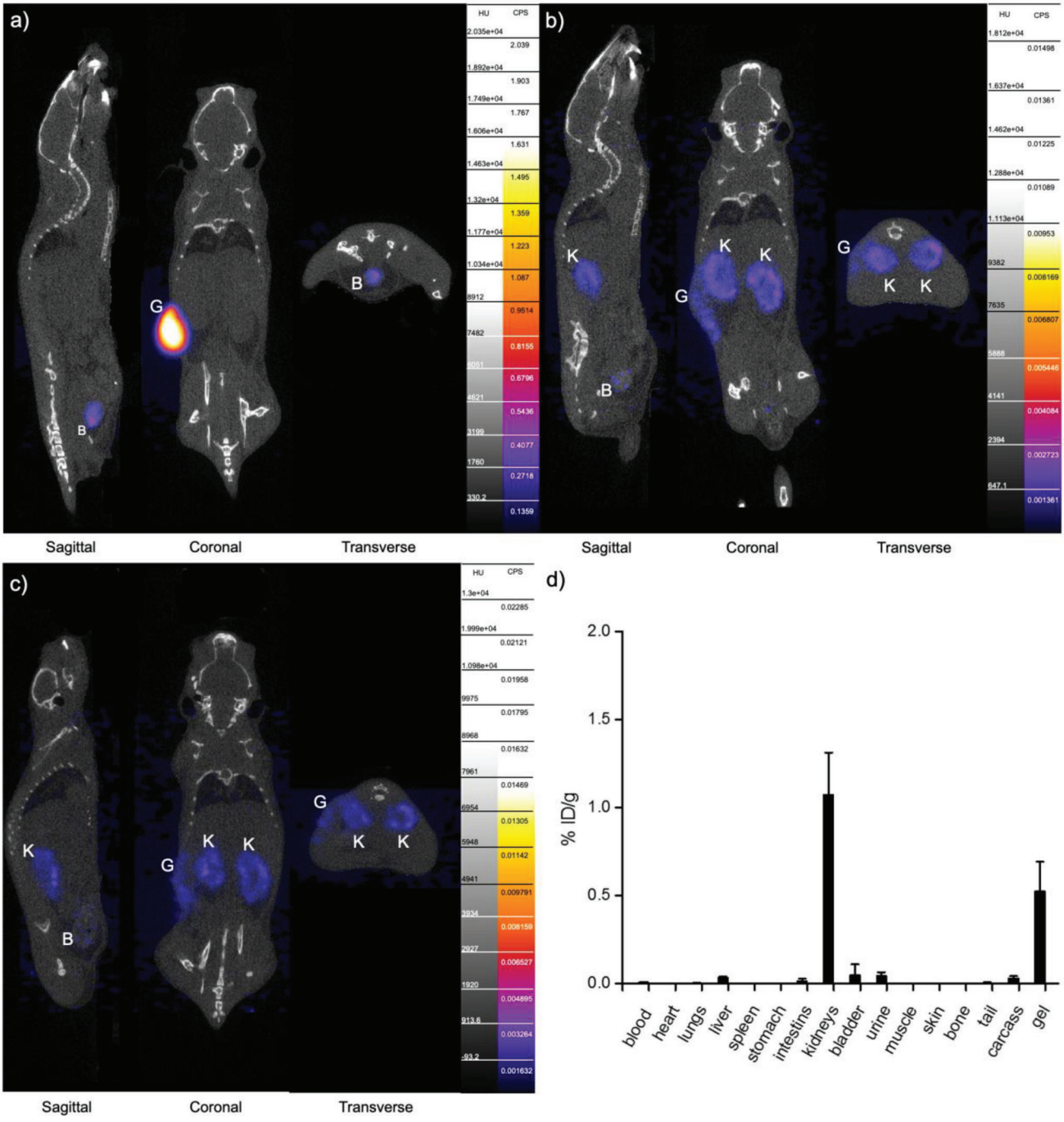

Figure 6. Histological assessment by H&E staining of local inflammation response in the skin tissues surrounding hydrogel implants (after 14 days). a) *PF-A* group; b) *PF-A + AuNPs* group; c) negative control skin. Cell nuclei appear in blue, while cytoplasm, elastin, and collagen are in pink. The gels are pointed with dashed arrows, whereas the slight presence of inflammatory cells at the surface of hydrogel volumes is pointed to with solid arrows. Ep: epidermis; D: dermis; A: adipose tissue; M: muscle; C: conjunctive tissue. The thickness of the slice is 5 µm.

its physicochemical characteristics, a polymer system can take 1–2 min to fully transition to a solid or semi-solid state.[40] As a consequence, some amount of encapsulated compounds can be lost during gel formation and eliminated by the body.[41] This rapid elimination of AuNPs by the kidneys would likely be slowed down for hydrogels that are cross-linked before insertion in the body. Therefore, based on these observations, we modified the hydrogel preparation procedure by incorporating a cross-linking process before implantation in animals, as described in the final part of this study.

Between day 1 and day 2, the signal in the hydrogel implants ([^{89}Zr]Zr-AuNPs) gradually faded out (coronal view in Figure 7,

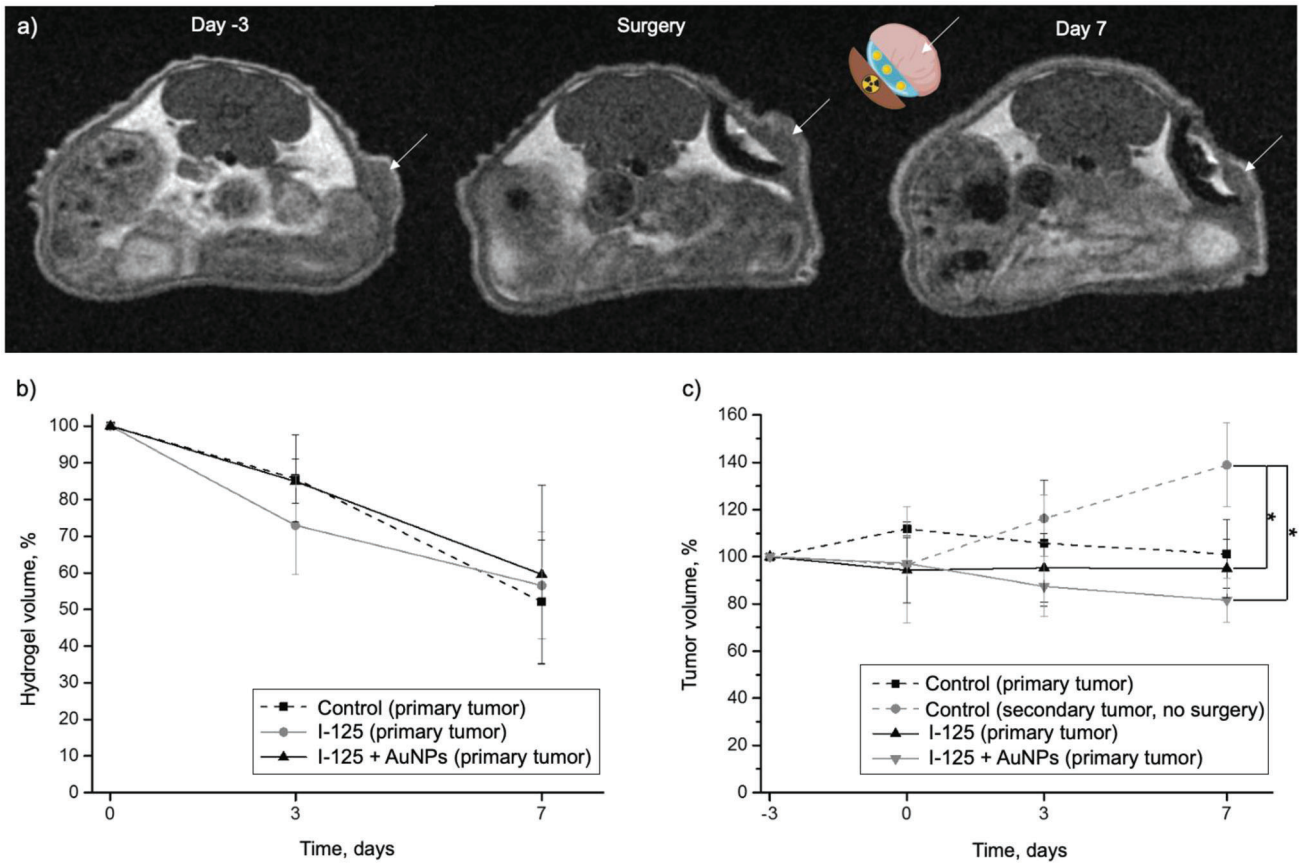

Figure 7. AuNP release study by PET, from s.c. injected hydrogels at a) 30 min post-injection (p.i.); b) day 1 p.i., c) day 2 p.i. B – bladder, G – gel, K – kidneys. d) Ex vivo biodistribution study at 2 days p.i.

panels b and c), confirming the efficient short-term release of AuNPs. These data align with the findings of a previous in vitro release study conducted with the same hydrogel formulation exposed to simulated vaginal fluid. In those conditions, it was demonstrated that ≈80% of AuNPs were released within just 2 days of incubation.[30]

The present data also point out to an excretion of [^{89}Zr]Zr-AuNPs through the kidneys and bladder with urine (sagittal and transverse views in Figure 7, panels b and c), which is expected for ultra-small nanoparticles. In applications requiring the in vivo administration of metallic NPs, very small hydrodynamic diameters are often preferred as these particles can be excreted from the body by renal clearance, which avoids the risk of NP accumulation in the organs such as the spleen and liver that could cause long-term toxicity.[15]

An ex vivo biodistribution study was performed on day 2 (48 h +/− 2 h) (Figure 7, panel d) and demonstrated that only a low amount of the [^{89}Zr]Zr-AuNPs was left in the kidneys (1.08 ± 0.24% ID g^{-1}) and the residual gel (0.53 ± 0.17% ID g^{-1}). These data corroborate the PET signal results. To demonstrate that the detected signal on the PET scans indeed corresponds to the [^{89}Zr]Zr-AuNPs and not to [^{89}Zr]Zr-Deferoxamine B (DFO), a potential metabolite of [^{89}Zr]Zr-AuNPs, elemental analysis measurements by microwave plasma atomic emission spectrometry (MP-AES) were performed with samples of the urine and kidneys. A concentration of Au in the order of 0.06 ± 0.02 mmol L^{-1} (or 29.12 ± 12.88% ID g^{-1}) was found in the urine samples, whereas the value found in the kidneys was 1.35 ± 0.47% ID g^{-1}. These data corresponded well with the results of the ex vivo biodistribution study (radioactivity counting measurements) and confirmed the presence of the administered AuNPs in the kidneys and urine samples and their excretion pathway through the kidneys.

3.3. AuNP-Releasing Hydrogels Applied as a 3D-Printed Subcutaneous Implant: Radiosensitizing Effect on Tumors

A radioactive BT implant and an AuNP-containing hydrogel cushion were specifically designed to measure in vivo the impact of radiosensitizing agents when tumors were irradiated with low-energy photons. Lens-shaped PF127-alginate hydrogel cushions were 3D-printed as described in Methods, Section 2.2.5, and tailored to the size and shape of each tumor to be treated in mice. The cushion was then applied to a 3D-printed PEEK BT insert containing an iodine-125 (^{125}I, 28.4 keV average energy, 59.4-day half-life) seed, which served as the radioactive source. These tailored implants were inserted surgically at the surface of the tumor. A schematic representation of the original brachytherapy tool developed for this study can be found in Figure 1,

while the experimental groups are described in Methods, Section 2.2.5.

MRI scans of each mouse (Figure 3, panel a) were used to monitor the size of tumors and the residual thickness of hydrogel cushions at selected time points. The BT PEEK inserts appeared as dark arches on the MRI scans, with the radioactive seed producing a slight image artifact in the middle (Figure 3, panel a, the surgery day). The 3D-printed hydrogels were visible as bright white structures lining these dark arches, thanks to the inclusion of biocompatible ultra-small iron oxide nanoparticles (USPIONs) in the hydrogel during the 3D-printing process (Methods, Sections 2.2.2 and 2.2.5) that provided a "positive" contrast effect compatible with T_1-weighted MRI imaging.[42] The tumors appeared as a gray mass (white arrows in Figure 3, panel a). The contrast between the tumor mass, hydrogel cushion and solid polymer (PEEK) BT inserts enabled excellent delineation of each component, which allowed for monitoring of the implant position relative to the tumor and quantifying hydrogel and tumor volumes at different time points.

The hydrogel volumes decreased uniformly across the three groups: I-125 + AuNPs (*PF-A + AuNPs* in the presence of a ^{125}I-source), I-125 (*PF-A* hydrogel in the presence of a ^{125}I-source), and control (surgery, *PF-A* hydrogel only) (Figure 3, panel b). For instance, on day 3 after the surgery, the hydrogel's volume was found to be 85.0 ± 6.0%, 73.0 ± 13.5% and 85.8 ± 11.9% for the I-125 + AuNPs, I-125 and control (primary tumor) groups, respectively. By comparison with the results from the in vivo s.c. hydrogel administration study (Figure 4, panel b), which demonstrated a very steep decrease in hydrogel volumes in 3 days, the degradation of the 3D-printed hydrogel proceeded more slowly. This fact could be explained by the limited exposure of the hydrogel to biological fluids as a result of the presence of the PEEK BT insert that acts as a physical barrier. The hydrogel cushions remained entirely visible throughout the experiment. On day 7 post-surgery, the hydrogel's volumes were 60.0% ± 24.3%, 56.6% ± 14.7% and 52.1% ± 17.0% of the initial volumes for the I-125 + AuNPs, I-125 and control (primary tumor) groups, respectively.

The tumor volume was also monitored over the 7-day experiment (Figure 3, panel c). It is important to note that the goal of this experiment was not to control the tumor volume. To achieve this, multiple ^{125}I seeds would have been necessary, which would have led to tissue necrosis. Using a high amount of radioactivity would have altered the tumor morphology to the extent that it would have been difficult to detect ROS in these tissues, which was one of the main goals of this study.

The presence of only one radioactive seed in the tumor's vicinity did not substantially affect the tumor's total volume. Throughout the experiment, the tumor volume in all groups of animals that underwent surgery remained relatively similar. Interestingly, the secondary tumors on the other flank of the same animals, not exposed to the surgery (in Figure 3, panel c, "control, secondary tumor, no surgery"), were found to increase in volume, and this increase was statistically significant compared to the surgery groups at day 7 of the experiment. This suggests that the surgery affected the tumor growth, possibly due to its invasive nature and the polymer implant both potentially disrupting the vasculature that irrigates the tumor.

The presence of AuNPs in cancer tissue irradiated by a BT device is expected to generate a high concentration of ROS, which may have a poisoning effect on tumor cells. To verify this hypothesis, ROS concentration was visualized in histological sections of the tumor samples harvested on day 7 (**Figure 8**).

As expected, there was no AuNPs signal in the I-125 and control groups (Figure 8, panels e and f). However, the tumor from the I-125 + AuNPs group displayed a strong signal, indicating the diffusion of AuNPs into the tumor volume (Figure 8, panel d). The generation of ROS was detected by dihydroethidium (DHE) staining (Figure 8, panels g–i). DHE reacts with ROS to produce oxidation products detectable as red fluorescence.[43,44] Red fluorescence was nearly absent in the tumors from the control group (Figure 8, panel i). In the tumors from the I-125 group, a red signal was detected, confirming radiation-induced ROS production (Figure 8, panel h). A remarkable red fluorescence signal was also found in the I-125 + AuNPs group, which colocalized with the AuNP signal (Figure 8, panel g), indicating significant ROS production in the tumors due to the interaction between the released AuNPs and the radiation from the ^{125}I seed.

The extent of ROS and AuNP signal colocalization was further investigated in this specific group (I-125 + AuNPs) using histology slices taken deeper into the tumors (**Figure 9**). The presence of AuNPs was observed up to the fifth slice, corresponding to the depth of 100 µm from the tumor surface (Figure 9, panels a and b). Beyond 100 µm, the signal intensity decreased sharply, almost to the background levels. These results suggest that the AuNPs, released by the hydrogel on the surface of tumors, penetrated deeper into the cancerous tissue but diffused only to a limited depth (Figure 9, panel b).

The presence of AuNPs in the first 100 µm resulted in a strong red fluorescence signal corresponding to ROS. The two signals were found to be colocalized, indicating that the ROS population was generated in close proximity to AuNPs as a result of their interactions with the radiation. In contrast to AuNPs, the ROS signal, although less intensive, was detected at a deeper range within the tumor. It faded gradually throughout the tumor depth, decreasing by 50% at 500 µm depth and by 80% at 1000 µm depth. It is worth noting that the ROS signal intensity beyond the AuNP distribution (beyond 100 µm in tumor depth) was comparable to that observed in the I-125 group (as shown in Figure 8, panel h). Therefore, it is likely that this ROS population was generated by the direct interaction of radiation with water molecules without the contribution of AuNPs. According to the Monte Carlo simulations (described in Methods, Section 2.2.5), the absorbed dose and photon fluence from ^{125}I seeds decreased only by ≈30% at a depth of 1500 µm in tumors (as shown in Figure 9, panel c), enabling the production of ROS at those depths. This is possibly the first quantitative study that confirms in such a graphical manner the impact of AuNPs on ROS production in tumors irradiated by low-dose-rate BT implants.

4. Discussion

The potential of AuNPs as effective radiosensitizers in BT applications, including for the treatment of cervical cancer, has been highlighted in recent years.[11,45–53] When injected in cancer tissues irradiated by BT, AuNPs interact with the low-energy photons emitted by the radioactive source and produce low-energy species, such as Auger electrons, secondary photons and photoelectrons.[11] Photoelectric absorption is the dominant

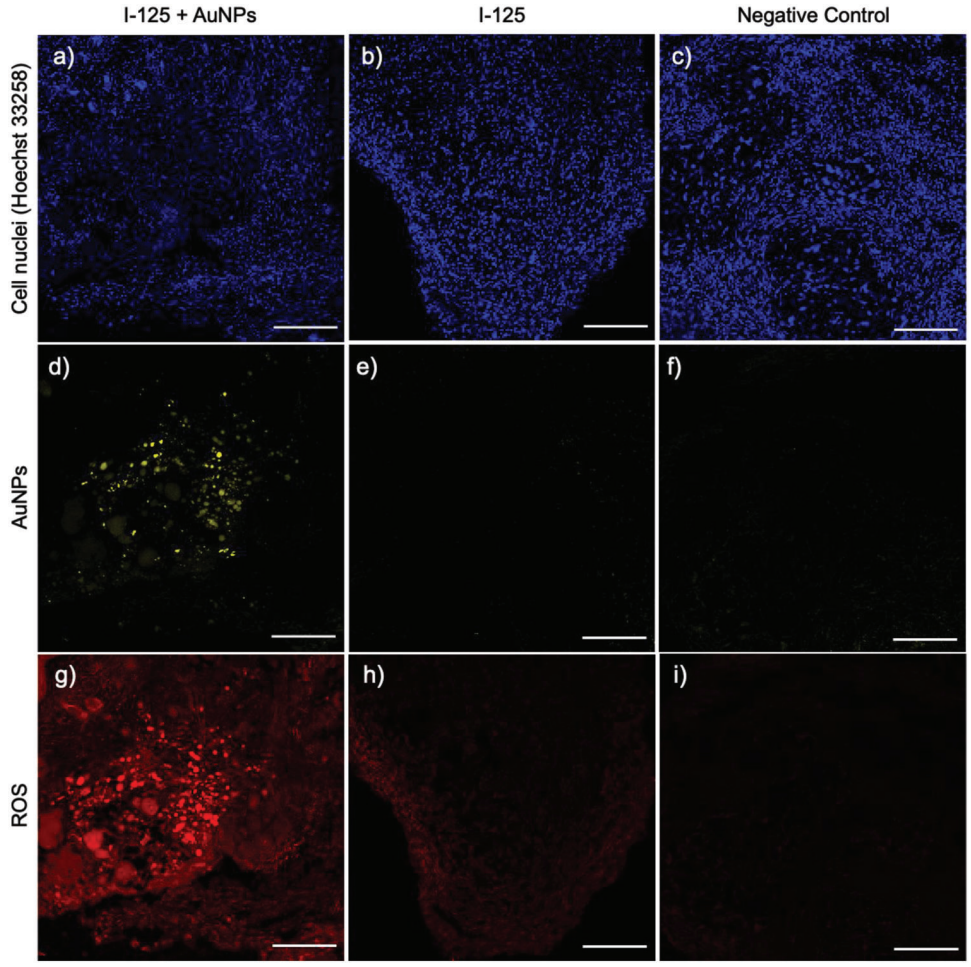

Figure 8. Immunofluorescence analysis of the tumor samples from the groups I-125 + AuNPs (a, d, g), I-125 (b, e, h), and negative control (c, f, i) on Day 7 post-surgery, the slice thickness is 20 µm, the scale bar is 500 µm.

interaction process between high-Z atoms and photons in the lower energy range (i.e., ≤50 keV). These multiple emissions, although of low energy, greatly enhance the dose deposited in the immediate vicinity of AuNPs. The mechanisms underlying the radiosensitization effect by AuNPs can be classified into three categories or phases: the physical phase, the chemical phase, and the biological phase.[48,54] The low-energy emissions activate the production of ROS, which are toxic to cancer cells, making this one of the most important mechanisms of action of these radiosensitizers.[51,55,56]

The optimal size for AuNPs as radiosensitizers is estimated to be around 5 nm to maximize cellular uptake, facilitate diffusion in tumors, and enhance renal clearance.[51] Catalytic reactions, which occur at the electronically active surfaces of AuNPs, are one of the well-documented chemical contributions to radiosensitization.[57] The effect of these catalytic reactions on radiosensitization is more prominent in small-sized AuNPs with a greater surface area-to-volume ratio.[57] The surface of AuNPs can mediate the transfer of electrons from surface-bound donor groups to molecular oxygen, which leads to the generation of free radicals and ROS on the surface of the AuNPs.[48] In turn, the ROS can damage DNA, proteins, and lipid membranes via oxidation.[51,55,56] Moreover, the cellular internalization and radiosensitization effect of spherical AuNPs is known to be greater than rod, cubic, prismatic, and star-shaped ones of similar size.[58–60]

The administration route of AuNPs as radiosensitizers is an essential factor for their application. In this study, we exploited the accessibility of cervical cancer to evaluate hydrogel formulations that could be applied topically to the vaginal mucosa as a delivery vehicle for AuNPs. Evidence abounds in the scientific literature on the use of PF127 combined with alginate for wound healing applications. PF127, the main component of the developed hydrogel, is approved by the FDA and Health Canada for dental, nasal and topical routes of administration.[61] It is also listed in the US and European Pharmacopoeia as a gelling agent for vaginal formulations (a maximum permissible concentration is 50% w/w).[62] However, the mechanisms by which PF127-alginate formulations degrade in vivo have yet to be thoroughly investigated.[63,64] PF127-alginate hydrogel degradation depends on parameters such as components concentration, molecular weight, the viscosity and L-guluronic acid content in alginate, the ionic cross-linking agent and gelation rate. Because of this complex set of variables, comparison between different

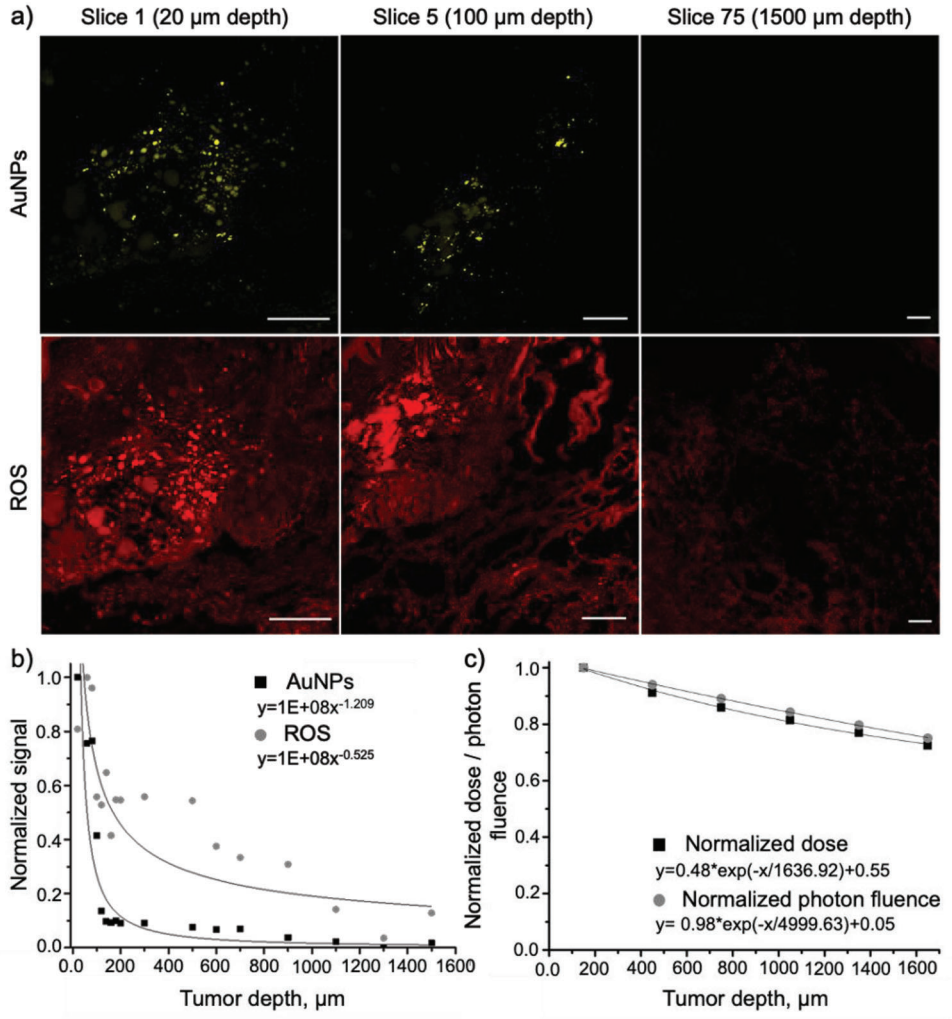

Figure 9. Detection of AuNPs and ROS (fluorescence) at different depths of the tumor mass after treating it with BT in the presence of AuNP-containing hydrogel (i.e., ^{125}I + AuNPs group). a) Representative immunofluorescence images of several slices of the sample showing AuNPs and ROS signals (slice thickness 20 μm; scale bar 500 μm). The images at 20 μm (Slice 1) were reused from the Figure 8, panels d,g; b) Distribution of AuNPs and ROS signals across the depth of tumors (fitted to the power trendline); c) Distribution of the absorbed dose and photon fluence across the depth of tumors from the ^{125}I seed (extracted from the Monte Carlo simulations, normalized, and fitted to the exponential trendline).

studies is difficult. For instance, Abdi et al. injected s.c. in the BALB/c nu/nu mice a PF127 (25% w/v) – alginate (3% w/v, low viscosity) hydrogel pre-cross-linked with 0.2% $CaSO_4$; they observed that only traces of this formulation were left after 7 days.[65] Fu et al. developed a nanocomposite hydrogel composed of PF127 (18% w/v), alginate (0.5% w/v, viscosity unknown), and hydroxypropylmethyl cellulose (0.5% w/v), which, once administered by s.c. injection, almost completely dissolved after 14 days.[66] This timeline is in agreement with the results of our study. Compared to these earlier studies performed qualitatively and post-mortem, the current study employed a non-invasive imaging technology (MRI), which allowed visualizing the implants at different time points by using each animal as its control. A quantitative degradation profile was extracted for each implant with reduced variability in the overall results.

The foreign-body reaction induced by s.c. administration of the PF127-alginate hydrogel formulation was evaluated by blood tests (general inflammation response) and in the harvested tissues from the implantation site (local inflammation response). The results of the current study indicate only mild local inflammation and no apparent systemic inflammation. Overall, these results appear similar to that of Fu et al., who investigated the biocompatibility of s.c. injected PF127-alginate-hydroxypropylmethyl cellulose; they found no necrosis, edema or hemorrhage in the surrounding tissue at 10 min, 2 days and 4 days after injection.[66] Seven days after injection, a slight increase in neutrophils was observed in the tissue, suggesting mild acute inflammation, which gradually decreased with time.[66]

When injected s.c., Pluronic F127 (M_w of 12.6 kDa) is excreted by the kidneys.[67] Akash et al. observed no PF127-induced alteration in the normal histology of the skin and kidney of the treated rats upon continuous administration of PF127 for one month.[67] The elimination profile of alginate drastically depends on its molecular weight and ratio of the (1,4)-linked β-D-mannuronate

and α-L-guluronate residues.[68,69] Low molecular weight alginate (≤48 kDa) can be excreted through renal filtration within 24 h.[69] In contrast, the clearance of high molecular weight alginate (530 kDa) occurs through the kidney and liver and is almost complete by day 14 of the study.[68] It is noteworthy that the administration of high molecular weight alginate also demonstrates an uptake by macrophages in the spleen over a 14-day period.[68] In this study, medium molecular weight alginate (100–250 kDa) was used; therefore, it is likely excreted through the kidney and liver. Since the hydrogel formulation was developed to be administered on the cervix wall, it is expected to be cleared from the body naturally with the vaginal discharge. Therefore, the metabolism and clearance of the Pluronic F127-alginate hydrogel were not investigated experimentally in this paper.

The capacity of the hydrogel formulation to release AuNPs was investigated by PET. PET is a highly sensitive non-invasive nuclear imaging technique that can provide in vivo quantitative information about various molecular processes and the status of targets.[70] The AuNPs (core size < 6 nm) co-administered (s.c.) with hydrogels were found to be released in just two days, which is ideal when a short-term release of a therapeutic compound is needed, such as in the case of cervical cancer brachytherapy. The PET scans revealed a fast elimination of the AuNPs by renal clearance. It is known that the size and the surface charge affect the biodistribution of NPs, with the smallest particles being eliminated by the kidneys and the larger ones accumulating in the spleen, liver, lungs and heart.[19] Alric et al. confirmed that ≈3 nm AuNPs radiolabeled with ^{99m}Tc and ^{111}In were eliminated by the kidneys.[71] The activity was found in the bladder in the first 30 min after the injection, with the kidneys and the bladder being the only organs visible on the scans after 75 h. Similar results were obtained in the present study, with a minimal accumulation of AuNPs in the liver and a strong signal in the urinary tracts (kidneys, bladder) after 48 h. Even though the developed hydrogel formulation is intended to be administered on the cervix wall, there is a possibility that released AuNPs could enter the main blood pool due to the rich blood circulation in the vagina. In such a case, the ultra-small size of the AuNPs would allow rapid excretion via the kidneys, thus avoiding undesired toxicity to vital organs.

The capacity of the PF127-alginate hydrogel to deliver AuNPs to cervical cancer (HeLa cells) induced in vivo in mice was demonstrated by an original approach developed specifically for this study and reported for the first time in this article. Hydrogel cushions were 3D-printed and tailored to the dimensions of cervical cancer tumors induced in the mice. These soft prints were placed on the 3D-printed solid BT implants, each containing one ^{125}I seed (0.75–0.89 mCi). These devices, designed and fabricated to mimic the insertion procedure of BT implants, were inserted by surgery beneath cervical cancer xenograft tumors. This procedure allowed for monitoring of tumor progression while offering more space to deploy the device compared with an orthotopic model. To our knowledge, this is the first study describing the development of a 3D-printed BT implant approach for preclinical studies in a mouse model.

^{137}Cs and ^{192}Ir are the two mainly used radioisotopes in cervical cancer brachytherapy. In the present work, ^{125}I sources (average energy 28.4 keV, half-life 59.4 days), widely employed in the treatment of prostate, eye and brain cancers, were used.[72] These sources are more readily available in clinical centers and are more affordable than their ^{137}Cs and ^{192}Ir counterparts. In addition, ^{125}I seeds are also used in cervical cancer therapy, more precisely as a new treatment regimen for recurrent cervical cancer.[73] Past studies suggest that its continuous low-dose-rate radiation causes much less damage to the healthy tissues around the tumor, resulting in improved success rates for the local control and low incidence of adverse effects compared to the high-dose-rate treatment with ^{192}Ir.[74] In addition, the dose enhancement effect induced by AuNPs distributed in tumor tissues is more effective under low-energy photon radiation such as that emitted by ^{125}I (maximum energy of 35 kV).[75]

In the present work, the short duration of the study (7 days) and the very minimal number of seeds ($n = 1$) did not cause a decrease in the tumor volumes treated by radiation. This observation is in agreement with the study performed by Li et al., who demonstrated that tumors treated with ^{125}I and ^{192}Ir decline in size only from day 28.[74] However, the main objective of this in vivo study was not to demonstrate the capacity to control tumor volume by coupling radiation and AuNPs, but rather to study the production of ROS in the vicinity of AuNPs irradiated by a flux of low-energy photons and to measure their diffusion in the cancer tissue. In a study fully dedicated to tumor volume control, the number of seeds and their precise localization in the tumor would be calculated prior to the experiments, similar to treatment planning in clinical low-dose-rate brachytherapy.

Here we confirmed that the tumor volumes containing AuNPs irradiated by ^{125}I produced a concentration of ROS detectable by confocal microscopy. ROS, in turn, can induce damage to the DNA, lipids and proteins, leading to mitochondrial dysfunction and, ultimately, tumor cell death.[48,76] The ROS and AuNP signals were visualized and quantified along the depth of the extracted tumor samples. We demonstrated that AuNPs were successfully released from the hydrogel delivery system and traveled in the tumor up to 100 µm, giving rise to a strong ROS signal along their way. Beyond the AuNP distribution, a weaker ROS signal was detected, which can be explained by the interaction of radiation and water molecules without the involvement of AuNPs. These results suggest that AuNPs, even if they do not travel very far in the cancer tissue, could be useful as topical post-surgery treatment—irradiated with low-energy photons—to eliminate the residual tumor cells located at the surface of the resection site (<1 mm thick margins). Revealing whether the synthesized AuNPs can generate radiation-induced ROS and their depth of penetration is a crucial step in developing clinical applications of AuNPs employed as radiosensitizers in brachytherapy. As an alternative to ^{125}I irradiation by seeds or plaque, AuNPs could be radiolabeled with alpha (α) or beta (β)-emitting radioisotopes already used for radiotherapy (e.g., actinium-225, lutetium-177).[77] Using radioactive AuNPs encapsulated into injectable or pre-formed degradable hydrogels could lead to innovative alternatives in long-term low-dose brachytherapy, in particular, to generate more localized radiation treatments in areas where precision is of prime importance.[78]

5. Conclusion

In this study, we developed a new procedure combining a low-dose-rate brachytherapy technology, the use of AuNPs as ra-

diosensitizers, and a topical gel (Pluronic F127 + alginate) applicable to cervical cancer therapy. First, the performance of the hydrogel delivery system, including its degradation, biocompatibility and ability to release the encapsulated AuNPs when administered in vivo, was evaluated. The results suggest that the developed hydrogel formulation is safe and can efficiently release AuNPs thanks to its optimal dissolution kinetics. Once released and distributed at the tumor surface, the AuNPs were proven to induce a robust production of ROS. Therefore, a combination of low-dose-rate brachytherapy and AuNP-releasing topical hydrogels represents an innovative and powerful approach to developing high-precision treatments for tumor margins and cancer tissues in geometrically challenging locations (e.g., in the vicinity of critical healthy tissues). The treatment strategy suggested in this work could significantly improve the efficacy of the post-surgical treatment of cervical cancer by killing the residual superficial tumor cells and decreasing the possibility of tumor recurrence.

Supporting Information

Supporting Information is available from the Wiley Online Library or from the author.

Acknowledgements

This study was partially financed by the NSERC-Discovery program (M.A.Fortin – RGPIN-2017-06173). M.K. received a fellowship from the NSERC-CREATE POND program (973111). The authors are grateful to the following researchers at Centre de Recherche du CHU de Québec: Julie Fradette and Dominique Mayrand for help in the histological assessment and immunofluorescence analysis, Sébastien Fortin and René C. Gaudreault (oncology axis) for providing HeLa cells used in the cell viability experiments and tumor inoculation. Vicky Dodier (Département de Génie des Mines, de la Métallurgie et des Matériaux, Université Laval) is acknowledged for her contribution to MP-AES analysis. PET/CT and MRI studies were performed at the small animal imaging platform (Centre de Recherche du CHU de Québec) with the help of Jenny Roy, Théophraste Lescot, and Marine Merlin. The authors acknowledge the flow cytometry core facility of the Centre de Recherche du CHU de Québec for their help in providing the data for this publication, especially Éric Boilard, Isabelle Allaeys and Etienne Doré. Baljeet Seniwal is acknowledged for performing the Monte Carlo simulations.

Conflict of Interest

The authors declare no conflict of interest.

Data Availability Statement

The data that support the findings of this study are available from the corresponding author upon reasonable request.;

Keywords

3D printing, brachytherapy, gold nanoparticles, hydrogels, localized vaginal delivery, radiosensitizers, reactive oxygen species

Received: January 29, 2023
Revised: April 18, 2023
Published online: May 14, 2023

[1] D. Singh, J. Vignat, V. Lorenzoni, M. Eslahi, O. Ginsburg, B. Lauby-Secretan, M. Arbyn, P. Basu, F. Bray, S. Vaccarella, *The Lancet Global Health* **2022**, *11*, 197.
[2] C. Federico, J. Sun, B. Muz, K. Alhallak, P. F. Cosper, N. Muhammad, A. Jeske, A. Hinger, S. Markovina, P. Grigsby, J. K. Schwarz, A. K. Azab, *Int. J. Radiat. Oncol., Biol., Phys.* **2021**, *109*, 1483.
[3] J. Abraham, J. L. Gulley, *The Bethesda Handbook of Clinical Oncology*, Lippincott Williams & Wilkins, Philadelphia, United States **2022**.
[4] X. P. Chao, X. C. Song, H. W. Wu, Y. You, M. Wu, L. Li, *Front. Oncol.* **2021**, *11*, 8.
[5] P. de la Puente, A. K. Azab, *J. Controlled Release* **2014**, *192*, 19.
[6] R. Banerjee, M. Kamrava, *Int. J. Women's Health* **2014**, *6*, 555.
[7] L. Li, X. X. Kou, X. J. Feng, M. C. Zhang, H. T. Chao, L. Y. Wang, *Radiat. Oncol.* **2015**, *10*, 6.
[8] D. Kim, Y. Ki, W. Kim, D. Park, J. Lee, J. Lee, H. Jeon, J. Nam, *Radiat. Oncol. J.* **2018**, *36*, 147.
[9] Y. L. Lai, Y. N. Jin, X. Wang, W. X. Qi, R. Cai, H. P. Xu, *Front. Oncol.* **2021**, *11*, 7.
[10] K. Haume, S. Rosa, S. Grellet, M. A. Śmiałek, K. T. Butterworth, A. V. Solov'yov, K. M. Prise, J. Golding, N. J. Mason, *Cancer Nanotechnol.* **2016**, *7*, 8.
[11] M. Laprise-Pelletier, T. Simão, M. A. Fortin, *Adv. Healthcare Mater.* **2018**, *7*, 1701460.
[12] S. Her, D. A. Jaffray, C. Allen, *Adv. Drug Delivery Rev.* **2017**, *109*, 84.
[13] R. Hu, M. Zheng, J. Wu, C. Li, D. Shen, D. Yang, L. Li, M. Ge, Z. Chang, W. Dong, *Nanomaterials* **2017**, *7*, 111.
[14] K. Song, P. Xu, Y. Meng, F. Geng, J. Li, Z. Li, J. Xing, J. Chen, B. Kong, *Int. J. Oncol.* **2013**, *42*, 597.
[15] P. Yadav, A. Bandyopadhyay, A. Chakraborty, S. M. Islam, K. Sarkar, *Gold Bull.* **2019**, *52*, 185.
[16] J. F. Dorsey, L. Sun, D. Y. Joh, A. Witztum, G. D. Kao, M. Alonso-Basanta, S. Avery, S. M. Hahn, A. Al Zaki, A. Tsourkas, *Transl. Cancer Res.* **2013**, *2*, 280.
[17] P. Singh, I. Mijakovic, *Expert Rev. Mol. Diagn.* **2021**, *21*, 627.
[18] P. Singh, S. Pandit, V. Mokkapati, A. Garg, V. Ravikumar, I. Mijakovic, *Int. J. Mol. Sci.* **2018**, *19*, 1979.
[19] R. Arvizo, R. Bhattacharya, P. Mukherjee, *Expert Opin. Drug Delivery* **2010**, *7*, 753.
[20] Z. Shi, Y. Zhou, T. Fan, Y. Lin, H. Zhang, L. Mei, *Smart Mater. Med.* **2020**, *1*, 32.
[21] Y. Zhang, F. Huang, C. Ren, J. Liu, L. Yang, S. Chen, J. Chang, C. Yang, W. Wang, C. Zhang, Q. Liu, X.-J. Liang, J. Liu, *Adv. Sci.* **2019**, *6*, 1801806.
[22] N. R. Welsh, R. K. Malcolm, B. Devlin, P. Boyd, *Int. J. Pharm.* **2019**, *572*, 118725.
[23] S. Gupta, M. K. Gupta, *Nano Rev. Exp.* **2017**, *8*, 1335567.
[24] F. Ordikhani, M. E. Arslan, R. Marcelo, I. Sahin, P. Grigsby, J. K. Schwarz, A. K. Azab, *Pharmaceutics* **2016**, *8*, 23.
[25] Q. Zhou, L. Zhong, X. Wei, W. Dou, G. Chou, Z. Wang, *Int. J. Pharm.* **2013**, *454*, 125.
[26] G. Jiang, X. Wang, Y. Zhou, C. Zou, L. Wang, W. Wang, D. Zhang, H. Xu, J. Li, F. Li, D. Luo, X. Ma, D. Ma, S. Tan, R. Wei, L. Xi, *Int. J. Nanomed.* **2021**, *16*, 4087.
[27] D.-y. Fan, Y. Tian, Z.-j. Liu, *Front. Chem.* **2019**, *7*, 675.
[28] H. J. Peng, Q. Huang, H. C. Yue, Y. Li, M. Wu, W. Liu, G. P. Zhang, S. Z. Fu, J. W. Zhang, *Int. J. Pharm.* **2019**, *556*, 97.
[29] S. J. Yu, C. L. He, X. S. Chen, *Macromol. Biosci.* **2018**, *18*, 13.
[30] M. Kiseleva, M. M. Omar, E. Boisselier, S. V. Selivanova, M. A. Fortin, *ACS Biomater. Sci. Eng.* **2022**, *8*, 1200.
[31] X. B. Chen, J. L. Zhang, K. T. Wu, X. H. Wu, J. Y. Tang, S. Q. Cui, D. L. Cao, R. L. Liu, C. Peng, L. Yu, J. D. Ding, *Small Methods* **2020**, *4*, 11.
[32] M. Killer, A. Schmitt, E. M. Keeley, G. M. Cruise, M. R. McCoy, *Neuroradiology* **2011**, *53*, 449.

[33] Y. J. Liang, A. Bar-Shir, X. L. Song, A. A. Gilad, P. Walczak, J. W. M. Bulte, *Biomaterials* **2015**, *42*, 144.
[34] J. Liu, K. Wang, J. Luan, Z. Wen, L. Wang, Z. L. Liu, G. Y. Wu, R. X. Zhuo, *J. Mater. Chem. B* **2016**, *4*, 1343.
[35] A. M. Bodratti, P. Alexandridis, *J. Funct. Biomater.* **2018**, *9*, 11.
[36] L. Schirmer, K. Chwalek, M. V. Tsurkan, U. Freudenberg, C. Werner, *Biomaterials* **2020**, *228*, 119557.
[37] P. A. Markov, D. S. Khramova, K. V. Shumikhin, I. R. Nikitina, V. S. Beloserov, E. A. Martinson, S. G. Litvinets, S. V. Popov, *J. Biomed. Mater. Res., Part A* **2019**, *107*, 2088.
[38] L. Zhang, Z. Q. Cao, T. Bai, L. Carr, J. R. Ella-Menye, C. Irvin, B. D. Ratner, S. Y. Jiang, *Nat. Biotechnol.* **2013**, *31*, 553-+.
[39] B. L. Ferreira, E. R. Ferreira, M. V. de Brito, B. R. Salu, M. L. V. Oliva, R. A. Mortara, C. M. Orikaza, *Front. Microbiol.* **2018**, *9*, 12.
[40] T. Li, M. Zhang, J. Wang, T. Wang, Y. Yao, X. Zhang, C. Zhang, N. Zhang, *AAPS J.* **2016**, *18*, 146.
[41] X. Wang, J. Wang, W. Wu, H. Li, *Drug Delivery* **2016**, *23*, 3544.
[42] Y. Gossuin, P. Gillis, A. Hocq, Q. L. Vuong, A. Roch, *Wiley Interdiscip. Rev.: Nanomed. Nanobiotechnol.* **2009**, *1*, 299.
[43] T. Yang, H. T. Ke, Q. L. Wang, Y. A. Tang, Y. B. Deng, H. Yang, X. L. Yang, P. Yang, D. S. Ling, C. Y. Chen, Y. L. Zhao, H. Wu, H. B. Chen, *ACS Nano* **2017**, *11*, 10012.
[44] C. Y. Yang, Y. D. Chen, W. Guo, Y. Gao, C. Q. Song, Q. Zhang, N. N. Zheng, X. J. Han, C. S. Guo, *Adv. Funct. Mater.* **2018**, *28*, 1706827.
[45] N. Goswami, Z. Luo, X. Yuan, D. T. Leong, J. Xie, *Mater. Horiz.* **2017**, *4*, 817.
[46] Y. Hua, J.-H. Huang, Z.-H. Shao, X.-M. Luo, Z.-Y. Wang, J.-Q. Liu, X. Zhao, X. Chen, S.-Q. Zang, *Adv. Mater.* **2022**, *34*, 2203734.
[47] T.-T. Jia, B.-J. Li, G. Yang, Y. Hua, J.-Q. Liu, W. Ma, S.-Q. Zang, X. Chen, X. Zhao, *Nano Today* **2021**, *39*, 101222.
[48] Y. Chen, J. Yang, S. Z. Fu, J. B. Wu, *Int. J. Nanomed.* **2020**, *15*, 9407.
[49] A. Khodadadi, H. A. Nedaie, M. Sadeghi, M. R. Ghassemi, A. Mesbahi, N. Banaee, *Appl. Radiat. Isot.* **2019**, *145*, 39.
[50] M. Laprise-Pelletier, J. Lagueux, M.-F. Côté, T. LaGrange, M.-A. Fortin, *Adv. Healthcare Mater.* **2017**, *6*, 1601120.
[51] M. Laprise-Pelletier, Y. Ma, J. Lagueux, M.-F. Côté, L. Beaulieu, M.-A. Fortin, *ACS Nano* **2018**, *12*, 2482.
[52] W. Ngwa, H. Korideck, A. I. Kassis, R. Kumar, S. Sridhar, G. M. Makrigiorgos, R. A. Cormack, *Nanomedicine* **2013**, *9*, 25.
[53] B. Seniwal, V. C. Thipe, S. Singh, T. C. F. Fonseca, L. F. de Freitas, *Front. Oncol.* **2021**, *11*, 766407.
[54] S. Penninckx, A. C. Heuskin, C. Michiels, S. Lucas, *Cancers* **2020**, *12*, 2021.
[55] F. Poignant, H. Charfi, C.-H. Chan, E. Dumont, D. Loffreda, É. Testa, B. Gervais, M. Beuve, *Radiat. Phys. Chem.* **2020**, *172*, 108790.
[56] R. Zhou, D. Zhao, N. M. Beeraka, X. Wang, P. Lu, R. Song, K. Chen, J. Liu, *Metabolites* **2022**, *12*, 943.
[57] S. Rosa, C. Connolly, G. Schettino, K. T. Butterworth, K. M. Prise, *Cancer Nanotechnol.* **2017**, *8*, 2.
[58] C. Carnovale, G. Bryant, R. Shukla, V. Bansal, *ACS Omega* **2019**, *4*, 242.
[59] B. D. Chithrani, A. A. Ghazani, W. C. W. Chan, *Nano Lett.* **2006**, *6*, 662.
[60] J. Li, J. E. J. Li, J. Zhang, X. Wang, N. Kawazoe, G. Chen, *Nanoscale* **2016**, *8*, 7992.
[61] G. Dumortier, J. L. Grossiord, F. Agnely, J. C. Chaumeil, *Pharm. Res.* **2006**, *23*, 2709.
[62] S. Garg, K. R. Tambwekar, K. Vermani, A. Garg, C. L. Kaul, L. J. D. Zaneveld, *Pharm. Technol.* **2001**, *25*, 14.
[63] H. Y. Chou, C. C. Weng, J. Y. Lai, S. Y. Lin, H. C. Tsai, *Polymers* **2020**, *12*, 2138.
[64] J. F. Cao, M. Z. Su, N. Hasan, J. Lee, D. Kwak, D. Y. Kim, K. Kim, E. H. Lee, J. H. Jung, J. W. Yoo, *Pharmaceutics* **2020**, *12*, 926.
[65] S. I. H. Abdi, J. Y. Choi, J. S. Lee, H. J. Lim, C. Lee, J. Kim, H. Y. Chung, J. O. Lim, *Tissue Eng. Regener. Med.* **2012**, *9*, 1.
[66] H. Fu, L. L. Huang, C. Q. Xu, J. L. Zhang, D. X. Li, L. Ding, L. Liu, Y. Dong, W. P. Wang, Y. R. Duan, *Nanomed.: Nanotechnol., Biol. Med.* **2019**, *21*, 102062.
[67] M. S. H. Akash, K. Rehman, H. Y. Sun, S. Q. Chen, *PLoS One* **2013**, *8*, e55925.
[68] A. A., N. L. Fletcher, Z. H. Houston, K. J. Thurecht, L. Grøndahl, *Carbohydr. Polym.* **2021**, *262*, 117947.
[69] A. Al-Shamkhani, R. Duncan, *J. Bioact. Compat. Polym.* **1995**, *10*, 4.
[70] D. L. Bailey, D. W. Townsend, P. E. Valk, M. N. Maisey, *Positron Emission Tomography*, Springer-Verlag London, London, United Kingdom **2005**, p. 382.
[71] C. Alric, I. Miladi, D. Kryza, J. Taleb, F. Lux, R. Bazzi, C. Billotey, M. Janier, P. Perriat, S. Roux, O. Tillement, *Nanoscale* **2013**, *5*, 5930.
[72] S. H. Wei, C. X. Li, M. Y. Li, Y. Xiong, Y. L. Jiang, H. T. Sun, B. Qiu, C. J. Lin, J. J. Wang, *Front. Oncol.* **2021**, *11*, 24.
[73] L. Han, C. L. Li, J. Y. Wang, X. Q. He, X. Zhang, J. D. Yang, G. F. Liu, *J. Cancer Res. Ther.* **2016**, *12*, C176.
[74] H. X. Li, J. Zhao, K. Shen, J. X. Yang, F. Q. Zhang, J. Chen, *Arch. Gynecol. Obstet.* **2014**, *289*, 1101.
[75] K. Yogo, M. Misawa, M. Shimizu, H. Shimizu, T. Kitagawa, R. Hirayama, H. Ishiyama, T. Furukawa, H. Yasuda, *Int. J. Nanomed.* **2021**, *16*, 359.
[76] S. Her, D. A. Jaffray, C. Allen, *Adv. Drug Delivery Rev.* **2017**, *109*, 84.
[77] S. Yook, Z. L. Cai, Y. J. Lu, M. A. Winnik, J. P. Pignol, R. M. Reilly, *J Nucl Med* **2016**, *57*, 936.
[78] S. Kim, S. G. Yim, A. Chandrasekharan, K. Y. Seong, T. W. Lee, B. Kim, K. Kim, S. Choi, S. Y. Yang, *J. Controlled Release* **2020**, *322*, 337.
[79] M. M. Omar, M. Laprise-Pelletier, P. Chevallier, L. Tuduri, M. A. Fortin, *Bioconjugate Chem.* **2021**, *32*, 729.
[80] W. C. Xiao, P. Legros, P. Chevallier, J. Lagueux, J. K. Oh, M. A. Fortin, *ACS Appl. Nano Mater.* **2018**, *1*, 894.
[81] D. Mayrand, J. Fradette, *Methods Mol. Biol.* **2018**, *1773*, 93.
[82] B. Faddegon, J. Ramos-Méndez, J. Schuemann, A. McNamara, J. Shin, J. Perl, H. Paganetti, *Phys. Med.* **2020**, *72*, 114.
[83] J. Perl, J. Shin, J. Schumann, B. Faddegon, H. Paganetti, *Med. Phys.* **2012**, *39*, 6818.
[84] F. Berumen, Y. Ma, J. Ramos-Méndez, J. Perl, L. Beaulieu, *Brachytherapy* **2021**, *20*, 911.
[85] M. J. Rivard, D. Granero, J. Perez-Calatayud, F. Ballester, *Med. Phys.* **2010**, *37*, 869.
[86] L. Qin, S. Yao, J. Zhao, C. Zhou, T. W. Oates, M. D. Weir, J. Wu, H. H. K. Xu, *Materials* **2021**, *14*, 408.
[87] M. Zankl, *Hoken Butsuri* **2010**, *45*, 357.